Robust effects of corticothalamic feedback during naturalistic visual stimulation

Martin A. Spacek[a,*], Gregory Born[a,b], Davide Crombie[a,b], Yannik Bauer[a,b], Xinyu Liu[a,b], Steffen Katzner[a,1], Laura Busse[a,c,1,*]

[a] *Division of Neurobiology, Department Biology II, LMU Munich, Munich, Germany*
[b] *Graduate School of Systemic Neurosciences, LMU Munich, Munich, Germany*
[c] *Bernstein Centre for Computational Neuroscience, Munich, Germany*

Abstract

Neurons in the dorsolateral geniculate nucleus (dLGN) of the thalamus are contacted by a large number of feedback synapses from cortex, whose role in visual processing is poorly understood. Past studies investigating this role have mostly used simple visual stimuli and anesthetized animals, but corticothalamic (CT) feedback might be particularly relevant during processing of complex visual stimuli, and its effects might depend on behavioral state. Here, we find that CT feedback robustly modulates responses to naturalistic movie clips by increasing response gain and promoting tonic firing mode. Compared to these robust effects for naturalistic movies, CT feedback effects on firing rates were less consistent for grating stimuli. Finally, while CT feedback and locomotion affected dLGN responses in similar ways, we found their effects to be largely independent. We propose that CT feedback and behavioral state use separate circuits to modulate visual information on its way to cortex in a stimulus-dependent manner.

Introduction

Mammalian vision is based on a hierarchy of processing stages that are connected by feedforward circuits projecting from lower to higher levels, and by feedback circuits projecting from higher to lower levels. Feedforward processing is thought to create feature selectivity [1, 2] and invariance to translation, scale, or rotation [2–5], to ultimately enable object recognition [6]. Hypotheses about the functional role of feedback circuits include top-down attention, working memory, prediction, and awareness [7–12]. Compared to theories of feedforward processing, however, there is little consensus on the specific function of feedback connections [13, 14].

*Correspondence: m.spacek@lmu.de (MAS), busse@bio.lmu.de (LB)
[1]Senior authors

Feedback in the mammalian visual system targets brain areas as early as the dorsolateral geniculate nucleus (dLGN) of the thalamus, where up to 30% of synaptic connections onto relay cells are established by corticothalamic (CT) feedback [15]. Direct CT feedback is thought to arise from V1 layer 6 (L6) CT pyramidal cells [16, 17], whose role in visual processing has remained elusive for a number of reasons. L6 CT pyramidal cells have notoriously low firing rates [18–23] and their deep location within cortex makes them a difficult target for *in-vivo* single cell functional imaging [24] and cell-type specific manipulations using optogenetics [25]. L6 CT pyramidal cells are also challenging to identify in extracellular recordings due to the heterogeneity of L6 neurons [16]. The action of CT feedback on dLGN activity is generally considered modulatory rather than driving [26], as CT feedback inputs contact the distal dendrites of relay cells via mGluR1 metabotropic receptors [27], implying rather slow and long-lasting effects on dLGN processing. Since L6 CT pyramidal cells provide both direct excitation and indirect inhibition of dLGN via the thalamic reticular nucleus (TRN) and dLGN inhibitory interneurons [17, 28], the effects of CT feedback are expected to be complex.

Despite the massive number of CT inputs to dLGN, the functional impact of CT feedback remains unclear [29, 30]. In the literature, diverse methods of manipulation with different temporal scales, specificity and overall sign (activation vs. suppression), have yielded diverse and even conflicting results. CT feedback, for instance, has been shown to modulate geniculate spatial integration [31–39], temporal processing [37, 40], response gain [38, 41–43], and transitions between tonic and burst firing modes [44, 45]. Other studies, however, found that manipulation of CT feedback did not change some or any of these dLGN response properties [25, 37, 46–48].

Most of these previous studies have probed the effects of CT feedback with artificial stimuli, and mostly in anesthetized animals; CT feedback, however, might be most relevant for processing of dynamic naturalistic information and during wakefulness. From a conceptual perspective, if the role of feedback was to provide context based on an internal model built from the statistics of the world [49–52], natural stimuli would be expected to best comply with this model, and hence better drive these feedback mechanisms. Indeed, it has previously been suggested that CT feedback might be more strongly engaged for moving compared to stationary stimuli [17], and for complex dynamic noise textures than simple moving bars [53], consistent with a potential role in figure-ground processing [33, 54, 55]. Furthermore, since the responsiveness of feedback projections [56, 57], including those originating from V1 CT neurons [30], seem to be strongly reduced by anesthesia, it is critical for an acceleration of our understanding to examine CT feedback effects in awake animals.

Here, we recorded spiking activity in dLGN of awake mice and investigated how CT feed-

back affected dLGN responses to naturalistic movie clips. In order to achieve reliable, temporally precise, and reversible suppression of CT feedback, we conditionally expressed channelrhodopsin2 (ChR2) in V1 parvalbumin-positive (PV+) inhibitory interneurons, whose activation can efficiently suppress cortical output [41, 58]. We found that V1 suppression had consistent modulatory effects on dLGN responses to movie clips, which could largely be captured by divisive transformations. Effects of CT feedback on dLGN responses to grating stimuli were more diverse, highlighting the stimulus-dependency of CT feedback effects. Finally, while geniculate responses during V1 suppression resembled those during quiescence, we found effects of CT feedback and behavioral state to be largely independent. Overall, our results demonstrate that visual information en route to cortex can be reliably modulated by extra-retinal influences such as cortical feedback and locomotion, which are likely conveyed via different modulatory pathways.

Results

CT feedback robustly modulates dLGN responses to naturalistic movie clips

To investigate the impact of CT feedback on visual processing of naturalistic stimuli, we presented to head-fixed mice full-screen movie clips and compared responses of dLGN neurons during optogenetic suppression of V1 activity to a control condition with CT feedback left intact (**Fig. 1**). The responses of individual dLGN neurons to naturalistic movie clips were characterized by distinct response events that were narrow in time and reliable across trials (**Fig. 1d, top**, example neuron). Consistent with the notion that CT feedback has a modulatory rather than driving role [59], even during V1 suppression the temporal response pattern remained discernible (Pearson correlation $r = 0.54$, $p < 10^{-6}$, **Fig. 1d,e**). Yet, as illustrated in the example neuron, with CT feedback intact, firing rates were higher and burst spikes were less frequent (**Fig. 1e, left**). As a consequence, the distributions of instantaneous firing rates in the two conditions were significantly different (KS test, $p < 10^{-6}$), and were more skewed during V1 suppression than with CT feedback intact ($\gamma = 2.02$ vs. 1.22; **Fig. 1e, right**).

We observed similar effects in the recorded population of dLGN neurons, where CT feedback enhanced overall responses and promoted tonic mode firing. Indeed, while mean firing rates varied almost 4 orders of magnitude across the population ($\sim$ 0.1–100 spikes/s), they were higher with CT feedback intact than with feedback suppressed (13.1 vs. 10.6 spikes/s; linear multilevel-model (LMM): $F_{1,173.1} = 12.5$, $p = 0.0005$; **Fig. 1f**). In addition, CT feedback also influenced more fine-grained properties of geniculate responses. First, with CT feedback, the mean proportion of spikes occurring as part of a burst event was about half of what we observed during suppression (0.050 vs. 0.090; LMM: $F_{1,177.9} = 45.6$, $p = 1.9 \times 10^{-10}$;

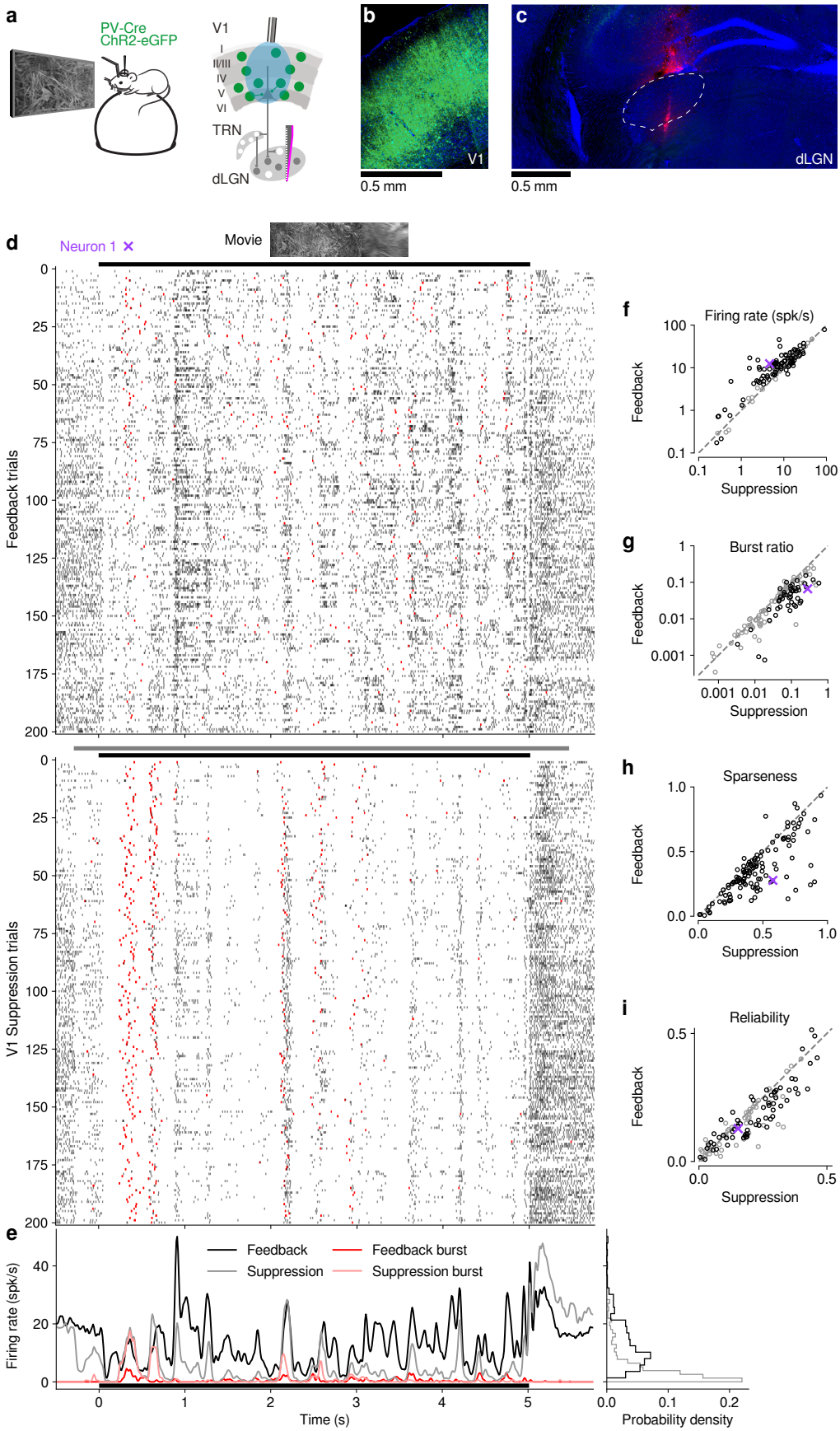
a
PV-Cre
ChR2-eGFP
V1
I
II/III
IV
V
VI
TRN
dLGN
b
V1
0.5 mm
c
dLGN
0.5 mm
d
Neuron 1
Movie
Feedback trials
V1 Suppression trials
e
Feedback
Suppression
Feedback burst
Suppression burst
Firing rate (spk/s)
Time (s)
Probability density
f
Firing rate (spk/s)
Feedback
Suppression
g
Burst ratio
Feedback
Suppression
h
Sparseness
Feedback
Suppression
i
Reliability
Feedback
Suppression

Figure 1 (**Previous page**) CT feedback modulates dLGN responses to full-screen naturalistic movie clips. (**a**) *Left*: Schematic of experimental setup. Head-fixed mice were placed on a floating Styrofoam ball and visual stimuli were presented on a screen located ~ 25 cm away from the animal. *Right*: ChR2 was conditionally expressed in PV+ inhibitory interneurons (*green*) in all layers of V1 using a viral approach. Extracellular silicon electrode recordings were performed in dLGN with and without optogenetic suppression of V1. (**b**) Coronal section close to the V1 injection site for an example PV-Cre mouse (*blue*: DAPI; *green*: eYFP; Bregma: -3.4 mm). (**c**) Coronal section at the dLGN (white outline) recording site, same animal as in (b). For post-mortem confirmation of the electrode position, the back of the probe was stained with DiI (*magenta*) for one of the recording sessions (*blue*: DAPI; Bregma: -1.82 mm). (**d**) Raster plots of an example neuron for 200 presentations of a 5 s naturalistic movie clip, with CT feedback intact (control condition, *top*) and during V1 suppression (*bottom*). *Red*: burst spikes; *black bar*: movie clip presentation; *gray bar*: V1 suppression. (**e**) *Left*: PSTHs for both the feedback (*black*) and V1 suppression (*gray*) conditions. Superimposed are PSTHs of burst spikes only, separately for feedback (*red*) and suppression (*pale red*) conditions. *Right*: Corresponding instantaneous firing rate distributions. (**f–i**) Comparison of CT feedback vs. suppression conditions for mean firing rate (f), burst ratio (g), temporal sparseness (h), and response reliability (i), all calculated for the duration of the movie clip. Sparseness captures the activity fraction of a neuron, re-scaled between 0 and 1 [60]. Response reliability is defined as the mean Pearson correlation of all single trial PSTH pairs [61]. For sample sizes, see **Table 1**. *Purple*: example neuron. Black markers in (f,g,i) indicate neurons with individually significant effects (Welch's t-test). See also **Fig. 1-Supplement 1** and **Fig. 1-Supplement 2**.

Fig. 1g). Second, consistent with the distributions of firing rate for the example neuron (**Fig. 1e, right**) and related to the relative increase of responsiveness in the population (**Fig. 1-Supplement 2d**), responses to the naturalistic movie clips with CT feedback intact were, on average, less sparse (0.35 vs. 0.54; LMM: $F_{1,170.1} = 55.4$, $p = 4.7 \times 10^{-12}$; **Fig. 1h**), indicating that neurons fired less selectively across the frames of the movie. Finally, we also examined the effect of CT feedback on response reliability. To quantify reliability, we computed the Pearson correlation coefficient of a neuron's responses between each pair of the 200 stimulus repeats per condition, and averaged the correlation coefficients over all pair-wise combinations [61]. With CT feedback intact, mean response reliability was lower than without feedback (0.15 vs. 0.18; LMM: $F_{1,166.9} = 22.5, p = 4.4 \times 10^{-6}$; **Fig. 1i**). Except for the effects on sparseness, the feedback effects on responses to naturalistic movies were unrelated to changes in firing rates (**Fig. 1-Supplement 2c–g**). The increased trial-to-trial reliability during V1 suppression could not be explained by higher stability in eye positions, because, first, variability in eye position was comparable between conditions with CT feedback intact vs. suppressed (**Fig. 1-Supplement 2h**), and second, effects of CT feedback on neural reliability were unrelated to changes in variability in eye position (**Fig. 1-Supplement 2i**). Splitting the dLGN population into putative cell types according to several functional characteristics and location within dLGN revealed few differences in how global V1 suppression affected firing rates and bursting (**Fig. 1-Supplement 3**). Finally, we repeated our experiments with more specific optogenetic suppression after selectively expressing the inhibitory opsin stGtACR2 [62] in V1 Ntsr1+ neurons, which correspond to $\geq 90\%$ to L6 CT neurons

[63, 64] (**Fig. 1-Supplement 4**). These control experiments with specific suppression of L6 CT neurons during viewing of naturalistic movies yielded identical conclusions (**Fig. 1-Supplement 4a–h**). Taken together, our results indicate that CT feedback can modulate responses of dLGN neurons to naturalistic movie clips. The modulations are consistent with a net depolarizing effect, which supports higher firing rates and more linear, tonic firing mode with higher dynamic range, at the expense of sparseness, trial-to-trial reliability, and signal-to-noise.

V1 suppression decreases dLGN responses to naturalistic movies by reducing response gain

To better understand the effects of V1 suppression on dLGN firing rate, we next asked whether the observed reduction in responsiveness could be explained by a divisive and/or subtractive change (**Fig. 2**). Using repeated random subsampling cross-validation, we fit a simple threshold linear model (**Fig. 2a**, *inset*) to timepoint-by-timepoint responses in suppression vs. feedback conditions, and extracted the slope and threshold of the fit for each subsample (**Fig. 2b,d**). In the two example neurons shown in **Fig. 2a–d**, the fitted slope was significantly smaller than 1 (neuron 2: median slope of 0.66, 95% CI: 0.63–0.69, **Fig. 2b**; neuron 1: median slope of 0.37, 95% CI: 0.32–0.41, **Fig. 2d**), while the threshold (x-intercept) was either small or not significantly different from 0 (neuron 2: median of 1.58, 95% CI: 0.39–2.91; neuron 1: median of -0.14, 95% CI: -1.49–0.89). We obtained similar results for the population of recorded neurons, where V1 suppression decreased the neurons' responses to naturalistic movie clips via a substantial change in response gain (slope of 0.76 ± 0.1; LMM) without a significant shift in baseline (threshold of 0.013 ± 1.3; LMM; **Fig. 2e**). This demonstrates that V1 suppression influences responses in dLGN to naturalistic movie clips predominantly via a divisive effect.

We noticed that the threshold linear model could predict the effects of V1 suppression better for some neurons than for others. We therefore explored whether poor fits of the model might be related to our finding that V1 suppression can trigger non-linear, burst-mode firing. For instance, the threshold-linear model accurately captured the responses of example neuron 2 (median $R^2 = 0.90$, cross-validated; **Fig. 2a,b**), which exhibited little bursting during V1 suppression (burst ratio: 0.007). Neuron 1, in contrast, had a higher burst ratio during suppression (0.28) and the prediction (*blue*) sometimes overestimated or underestimated peaks in the actual response (*gray*), such that the percentage of explained variability was rather low (median $R^2 = 0.29$, cross-validated, **Fig. 2c,d**).

Indeed, across the population of recorded cells, the model goodness of fit (median R^2, cross-validated) during V1 suppression was inversely related to the burst ratio (slope of -1.4 ± 0.23; LMM; **Fig. 2f**), consistent with the notion that the highly non-linear, all-

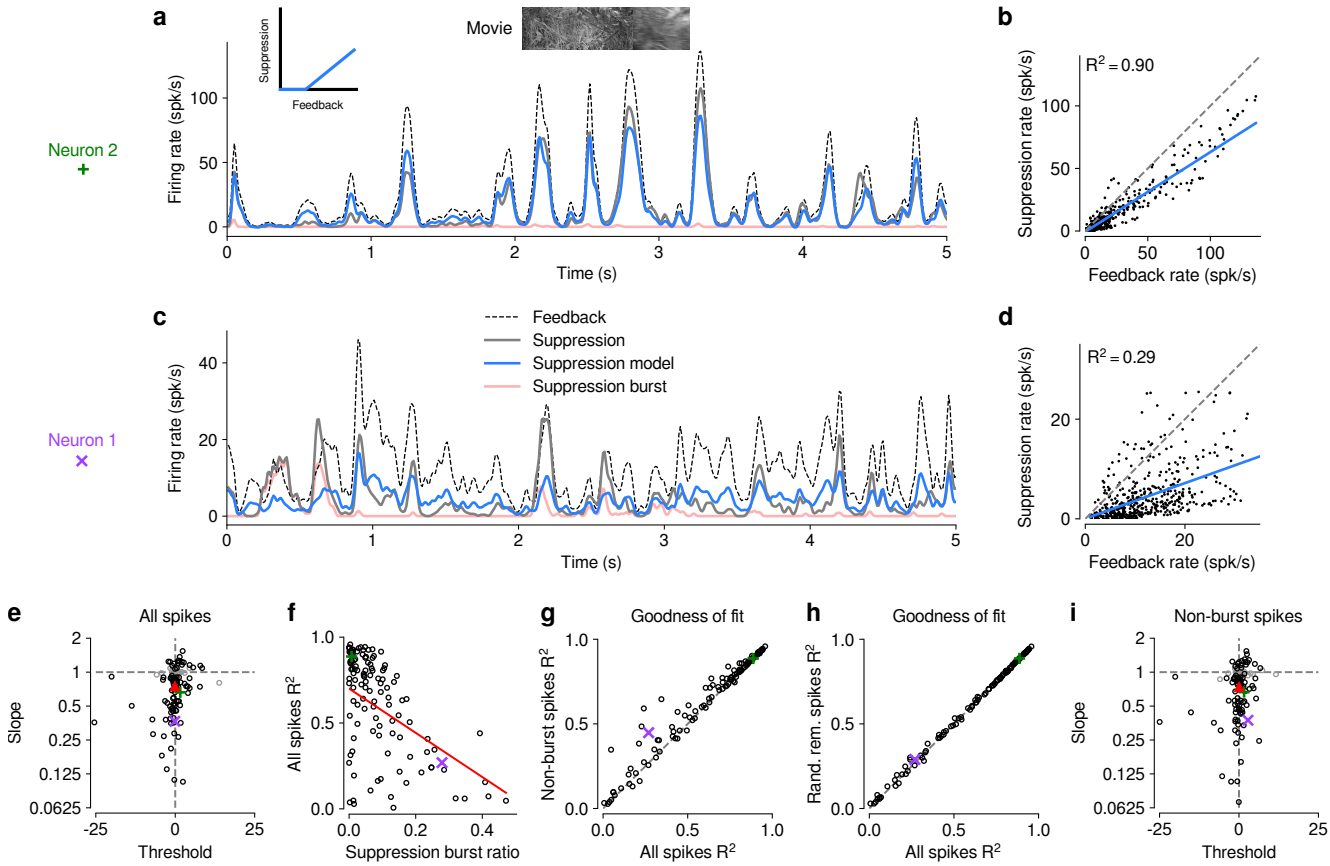

Figure 2 The effect of V1 suppression on dLGN responses to naturalistic movie clips is predominantly divisive.
(**a**) PSTHs of an example neuron during CT feedback (*black, dotted*) and V1 suppression (*gray*) conditions, for a random subset of 50% of trials per condition not used for model fitting. Responses during the suppression condition are approximated by the threshold linear model (*blue*) based on responses during the feedback condition. *Pale red:* PSTH during V1 suppression consisting only of burst spikes. *Inset*: cartoon of threshold linear model. (**b**) Timepoint-by-timepoint comparison of instantaneous firing rates of the PSTHs (derived from the 50% of trials not used for fitting) during the suppression vs. feedback conditions. PSTH data points are plotted at 0.01 ms resolution. *Blue line*: threshold linear model fit. (**c,d**) Same as (a,b) for a second example neuron (same as in **Fig. 1d,e**). (a,b) and (c,d) each contain data from 1 representative subsample. (**e**) Slope and threshold parameters for all neurons. Each point represents the median for each neuron across 1000 random subsamples of trials. Black points indicate neurons with slopes significantly different from 1 (95% CI). (**f**) Cross-validated model prediction quality (median R^2) vs. burst ratio during V1 suppression. *Red line*: LMM fit. (**g**) Model prediction quality with and without removal of burst spikes. (**h**) Model prediction quality with and without removal of an equivalent number of tonic spikes. (**i**) Same as (e) but with burst spikes removed. (e–h) *Purple, green*: example neurons; *red triangle*: LMM estimate of the mean.

or-none-like burst mode firing [65] cannot be captured by the threshold-linear model. To further investigate the impact of bursting on response transformations by CT feedback, we recomputed the PSTHs for each neuron during V1 suppression after removing all burst spikes. Removal of burst spikes allowed our model to capture the effects of V1 suppression even better (all spikes: mean $R^2 = 0.60$; non-burst spikes: mean $R^2 = 0.63$; LMM: $F_{1,152.8} = 5.9$, $p = 0.016$; **Fig. 2g**). Importantly, this increase in model performance was not simply a

consequence of removing a certain proportion of spikes that originally needed to be predicted: discarding an equivalent number of randomly selected tonic spikes did not yield improved fit quality (random tonic spikes removed: mean $R^2 = 0.60$; LMM: $F_{1,153.8} = 0.017$, $p = 0.9$; **Fig. 2h**). While burst spikes thus cannot be captured by the threshold-linear model, removing burst spikes did not change our conclusion that the effect of CT feedback on movie responses was predominantly divisive (slope: 0.75 ± 0.09; threshold: 0.22 ± 1.33; LMM; **Fig. 2i**), likely because burst events were much rarer than tonic spikes (see also **Fig. 1g**) [66]. Indeed, firing mode (all spikes vs. non-burst spikes) had no effect on either slope (LMM: $F_{1,153.7} = 0.57$, $p = 0.45$) or threshold estimates (LMM: $F_{1,150.5} = 0.21$, $p = 0.65$) of the simple linear model.

CT feedback modulates dLGN responses evoked by drifting gratings

Previous studies have investigated the effects of CT feedback using artificial stimuli, such as gratings and bars [25, 34, 41, 44]. To relate our findings to these studies, and to investigate the role of stimulus type, we next examined the effects of V1 suppression during the presentation of drifting gratings (**Fig. 3**). To approximate the visual stimulus configuration used for naturalistic movie clips, we presented full-screen gratings drifting in one of 12 different orientations, and selected a pseudo-random subset of trials for V1 suppression. As expected, we found that responses of single dLGN neurons in the control condition with CT feedback intact could be modulated at the temporal frequency (TF, 4 cyc/s) of the drifting grating (**Fig. 3a$_1$, b$_1$**). Similar to previous studies in mouse dLGN [67–69], we also encountered some dLGN neurons with tuning for grating orientation or direction (**Fig. 3a$_2$, b$_2$**).

Remarkably, V1 suppression had mixed effects on dLGN responses to drifting gratings. Example neuron 1, for instance, had lower firing rates with CT feedback intact, both in the orientation tuning (**Fig. 3a$_2$**) and the cycle-averaged response to the preferred orientation (**Fig. 3a$_3$**). In addition, with CT feedback intact, there were markedly fewer burst spikes. In contrast, example neuron 3 responded more strongly with CT feedback intact (**Fig. 3b$_2$, b$_3$**). Such diverse effects of CT feedback were representative of the recorded population (**Fig. 3c**): V1 suppression during grating presentation significantly reduced responses for some neurons, but significantly increased responses for others, such that the average firing rates in the two conditions were almost identical (feedback: 14.8 spikes/s, suppression: 15.1 spikes/s) and statistically indistinguishable (LMM: $F_{1,88.7} = 0.05$, $p = 0.83$). In contrast to these diverse effects on firing rate, but similar to our findings for naturalistic movie clips, intact CT feedback was consistently associated with less bursting (burst ratios of 0.041 vs. 0.15; LMM: $F_{1,90.8} = 42.6$, $p = 3.8 \times 10^{-9}$; **Fig. 3d**). Also similar to our findings for movies,

there was no relationship between the strength of feedback effects on firing rate and on bursting (**Fig. 4-Supplement 1a**).

Beyond studying overall changes in responsiveness and firing mode, we next asked how CT feedback affected the tuning for grating orientation of dLGN neurons. It is known from previous studies [67, 69–72] that mouse dLGN neurons show various degrees of orientation tuning, ranging from few strongly tuned neurons, potentially relaying tuned input from the retina [70], to a larger group with orientation bias [67, 72]. We computed orientation tuning curves separately for feedback and suppression conditions. For neuron 1, intact CT feedback was associated not only with lower average firing rates, but also poorer selectivity (OSIs of 0.14 vs. 0.25; **Fig. 3a**$_2$). In contrast, for neuron 3, orientation selectivity was similar during feedback and suppression conditions (OSIs of 0.1 vs. 0.09; **Fig. 3b**$_2$). These results were representative of the population, where CT feedback affected orientation selectivity in diverse ways, with virtually no difference in population means (feedback OSI: 0.13; suppression: 0.12; LMM: $F_{1,88.7} = 0.31$, $p = 0.58$; **Fig. 3e**; see also [25, 46, 47, 72]). For neurons with OSI > 0.02 and well-fit orientation tuning curves ($R^2 > 0.5$), preferred orientation during feedback and suppression conditions was largely similar, except for some cases where it shifted (**Fig. 3f**). As was the case for movie stimulation, for grating stimulation, splitting the dLGN population into putative cell types according to several functional characteristics and their location within dLGN revealed few consistent differences in how global V1 suppression affected firing rates and bursting (**Fig. 3-Supplement 1**). Taken together, although the effects of V1 suppression on firing rate seem more diverse in magnitude and sign for grating stimuli, the similarity of orientation selectivity between CT feedback conditions suggests underlying changes in gain, in accordance to what we observed for naturalistic movies.

Inspecting the spike rasters at different orientations, we realized that responses of geniculate neurons appeared to be more strongly modulated at the grating's temporal frequency during V1 suppression than when feedback was intact (**Fig. 3a**$_1$). To test whether V1 suppression affected the ability of dLGN neurons to follow the gratings' temporal modulation, for each neuron we computed the amplitude of the response at the stimulus frequency (F_1 component) relative to the mean response (F_0 component) [73, 74] and found that F_1/F_0 ratios were indeed lower when feedback was intact (1.08 vs. 1.22; LMM: $F_{1,90.5} = 15.8$, $p = 0.00014$; **Fig. 3g**). To explore the impact of CT feedback on the first harmonic response in more detail, we examined the cycle average responses to the preferred orientation, and asked how CT feedback affected response phase. Similar to the results obtained for the example neurons (**Fig. 3a**$_3$, **Fig. 3b**$_3$), we found that V1 suppression could advance response phase (**Fig. 3h**). This phase advance occurred more often for neurons whose responses during V1 suppression included a substantial proportion of burst spikes (**Fig. 3i**,

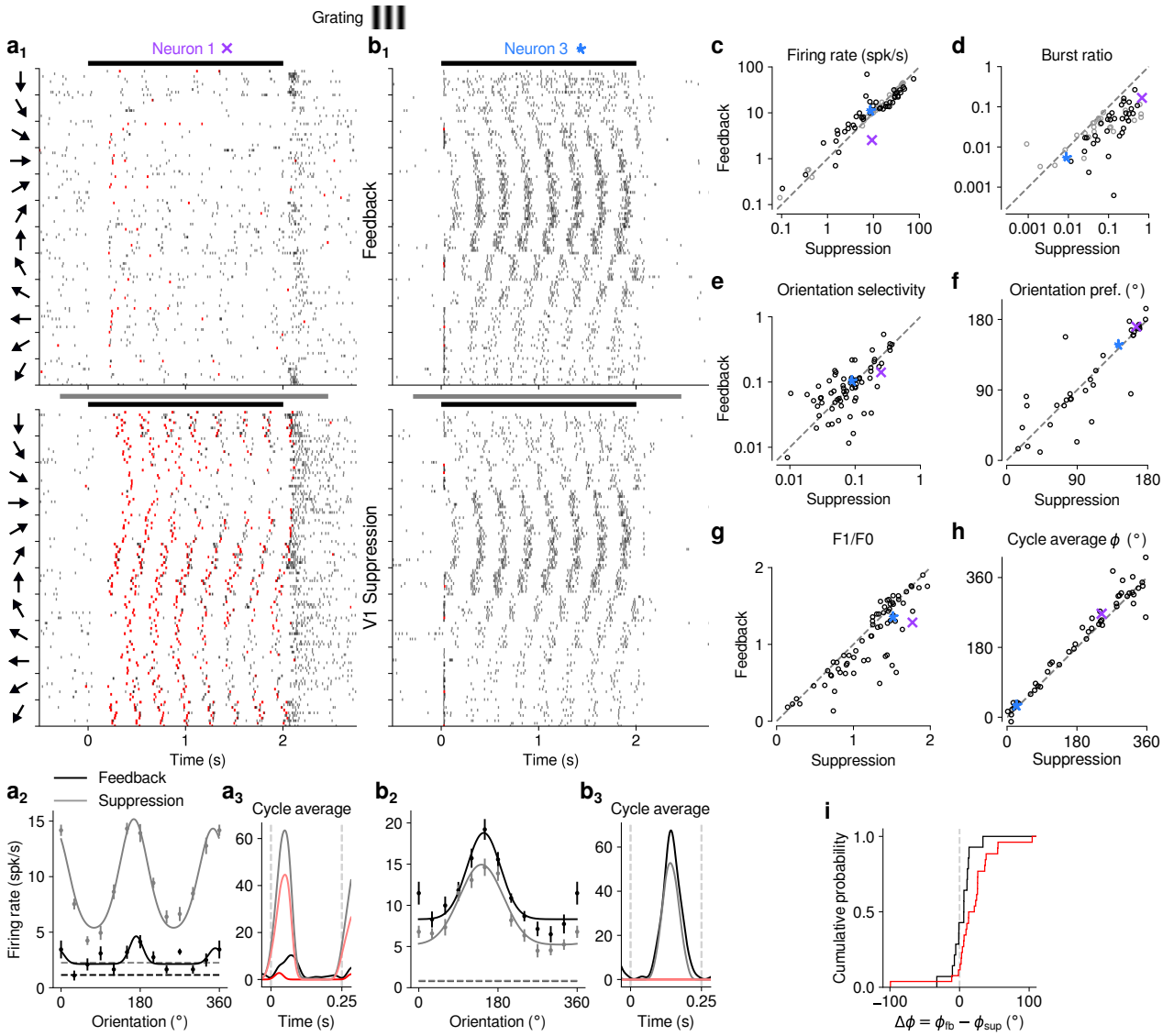

Figure 3 CT feedback modulates dLGN responses to drifting gratings.
(**a**) Responses of example neuron 1 (same as in **Fig. 1d,e** and **Fig. 2c,d**) to full-screen, drifting gratings. (**a**$_1$) Raster plot in response to drifting gratings, with trials sorted by grating orientation (10 trials per orientation, 30° steps). *Red*: burst spikes. (**a**$_2$) Corresponding orientation tuning curve. Dashed lines represent spontaneous firing rates in response to medium gray screen. *Error bars*: standard error of the mean. (**a**$_3$) Cycle average response to preferred orientation. *Black, gray*: cycle average constructed from all spikes. *Red, pale red*: cycle average constructed from burst spikes only. *Black, red*: CT feedback intact; *gray, pale red*: V1 suppression. (**b**) Same as (a), for example neuron 3. (**c–h**) Comparison of conditions with CT feedback intact vs. V1 suppression, for mean firing rate (c), burst ratio (d), orientation selectivity index (OSI) (e), preferred orientation θ (f), F_1/F_0 (g), and cycle average phase ϕ (h). *Purple, blue*: example neurons. Black markers in (c,d) indicate neurons with individually significant effects (Welch's t-test). (**i**) Cumulative distribution of cycle average phase differences between feedback and suppression conditions. *Black*: neurons with little burst spiking (ratio of cycle average peak for burst spikes to cycle average peak for all spikes < 0.1); *red*: neurons with substantial burst spiking (ratio of cycle average peak for burst spikes to cycle average peak for all spikes ≥ 0.1).

red; 25 of 29 neurons showed phase advance, $p = 0.0001$, binomial test) than for neurons whose V1 suppression responses had little or no bursting (**Fig. 3i**, *black*; 11 of 21 neurons advanced, $p = 1$, binomial test). Together with earlier work using intracellular recordings at different levels of holding membrane potential in anesthetized cats [75], these analyses demonstrate that the phase advance is driven by the dynamics of burst spiking. Finally, similar to our re-assessment of CT feedback effect on responses to naturalistic movies, our conclusions regarding the effects of CT feedback on grating responses did not change when we repeated our experiments using a selective suppression of Ntsr1+ neurons with stGtACR2 [62] (**Fig. 1-Supplement 4i–o**).

Effects of CT feedback on dLGN firing rates are more consistent and overall stronger for full-screen movies than full-screen gratings

Our analyses suggest that the impact of CT feedback on firing rates might be overall stronger for naturalistic movie stimuli than for gratings. To test this hypothesis, we focused on the subset of neurons recorded with both types of stimuli. Indeed, when we compared feedback modulation indices (FMIs) of firing rates, we found that FMI was on average more positive for movies than for gratings (0.15 vs. 0.053; LMM: $F_{1,38} = 5.21$, $p = 0.028$; **Fig. 4a**). Remarkably, in 10/39 neurons (**Fig. 4a**, dark lines) V1 suppression decreased firing rates for movies (positive movie FMI), but increased firing rates for gratings (negative grating FMI). The opposite effect only occurred in 3/39 neurons (dark dashed lines). These findings were not a consequence of differences in firing rates that might have already been present in conditions with CT feedback intact (**Fig. 4-Supplement 1b**), and were also not a consequence of the longer duration of V1 suppression during movie clips (**Fig. 4-Supplement 1c,d**).

Differences in CT feedback effects on firing rates to full-screen gratings and movies might be related to feedback-mediated changes in bursting, which might be stimulus-dependent [75, 76] and can drive high frequency firing. To test this hypothesis, we compared CT feedback modulation of burst ratio for gratings vs. movie clips, and found that V1 suppression indeed induced stronger bursting for gratings than for movies (**Fig. 4-Supplement 1e**). However, for both movies (**Fig. 1-Supplement 2c**) and gratings (**Fig. 4-Supplement 1a**), CT feedback effects on firing rates were unrelated to those on bursting. Thus, while suppression of CT feedback engages bursting overall more strongly for gratings than movies, this differential recruitment does not seem to account for differences in CT feedback-related modulations of firing rates for movies vs. grating stimuli.

Alternatively, CT feedback might operate differently on full-screen movie vs. grating stimuli, because the stimuli themselves might differentially engage CT feedback to modulate

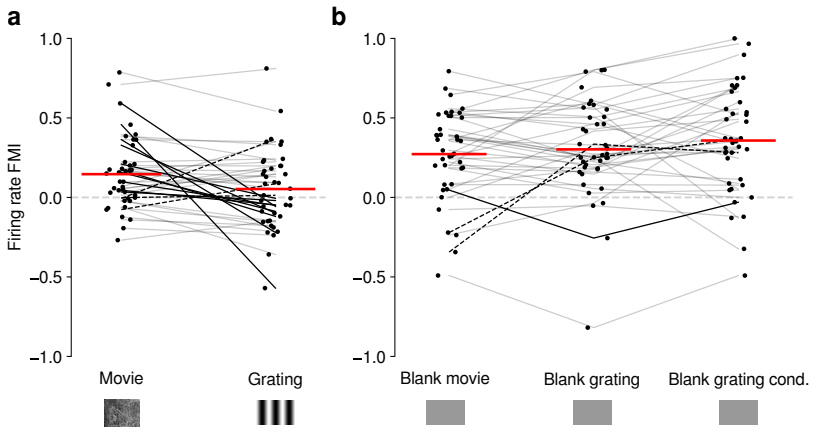

Figure 4 Effects of CT feedback on dLGN firing rate depend on stimulus type.
(**a**) Comparison of the strength of CT feedback effects on firing rate (feedback modulation index, FMI) during presentation of full-screen movie clips and gratings. (**b**) Comparison of the strength of CT feedback effect on firing rate for blank stimuli interleaved with movies or gratings. *Red*: mean (LMM), *dark lines*: changes in sign of feedback modulation effect with stimulus type from positive for movies to negative for gratings (*solid*) and vice versa (*dashed*). See also **Fig. 4-Supplement 1**.

dLGN processing. Differential engagement of CT feedback might be related to differences in multiple aspects of the two stimulus types, for instance contrast, spatial and temporal frequency, or spatial context. With respect to spatial context, a substantial body of literature has indicated that one role of CT feedback is to enhance dLGN center-surround antagonism [31–35, 37, 39, 77, 78]. Such center-surround antagonism might be stimulus dependent: recordings in area V1 have demonstrated that the strength of surround modulation dynamically changes with the statistics of naturalistic stimuli, and on average is less than the surround modulation exerted by large-sized iso-oriented gratings [79].

To test whether CT feedback effects differ for movies and gratings due to differential modulation of dLGN surround suppression, one would ideally compare responses to movies and gratings of optimal size, which evoke little surround suppression, in addition to responses to both types of full-screen stimuli, which evoke more surround suppression, all while manipulating CT feedback. However, due to limited recording time and the impracticality of centering movies and gratings over the retinotopically dispersed RFs in dLGN (**Fig. 1-Supplement 1b**) [67], we did not collect responses to optimally sized stimuli. However, our recordings did include periods of blank screen, which minimally recruit surround mechanisms. These were short (∼0.3 s) periods directly preceding each full-screen movie and grating trial (see e.g. **Fig. 1d** and **Fig. 3a**$_1$), as well as blank trials interleaved as one condition in the grating experiments. Applying our analyses to these various blank stimuli (**Fig. 4b**, **Fig. 4-Supplement 1g–i**), we found that CT feedback enhanced mean firing rates regardless of blank type or blank period duration (positive firing rate FMIs, mean FMIs: 0.27 vs. 0.30 vs. 0.36; LMM: $F_{2,76} = 1.69$, $p = 0.19$; **Fig. 4b**). This CT feedback-related average

enhancement for blank stimuli was even stronger than the enhancement observed during movie presentation (LMM: $F_{1,116} = 15.1$, $p = 0.0002$), and stronger than the mixed effects during grating presentation (LMM: $F_{1,116} = 34.9$, $p = 3.6 \times 10^{-8}$). Since the CT feedback effects on these various blank stimuli (see also **Fig. 4-Supplement 1e–l**) did not depend on blank period duration or whether blanks were embedded in grating or movie experiments, we interpret these findings to represent differential, stimulus-dependent engagement of CT feedback.

These findings are consistent with the interpretation that CT feedback most strongly enhances firing rates to blanks in both movie and grating experiments, because the recruitment of suppressive mechanisms via the indirect inhibitory CT feedback circuit is minimal. In contrast, presentation of iso-oriented full-screen gratings likely invokes stronger suppressive feedback mechanisms, such that overall CT feedback influences would be comprised of a mix of direct excitation and indirect inhibition. Suppressing cortex during presentation of full-screen gratings would thus result in reduced excitation, but also release from inhibition, such that the two effects on firing rate might cancel out. Finally, if indirect inhibitory influences of CT feedback were recruited less by full-screen naturalistic movies, CT feedback effects on firing rates would more strongly reflect the influences of the direct, excitatory CT feedback circuit. Taken together with previous studies in anesthetized cats demonstrating that CT feedback-mediated enhancement of dLGN surround suppression can depend on the orientation alignment of center and surround [33, 55], these findings suggest that the strength and sign of CT feedback gain might be stimulus-dependent and potentially sensitive to the statistics of the center and the surround stimulation.

Effects of locomotion on dLGN responses resemble effects of CT feedback, but are largely independent

Previous studies have reported that responses of mouse dLGN neurons to grating stimuli are modulated by locomotion [80–82]. To assess how these findings extend to more complex stimuli, we separated the trials with CT feedback intact according to the animals' locomotion behavior. When we examined the spike rasters and PSTHs of example neuron 1 in control conditions with CT feedback intact (**Fig. 5a,b**), we found that, despite preserved temporal features of the responses (Pearson correlation $r = 0.72$ between run and sit PSTHs, $p < 10^{-6}$), firing rates were higher overall during locomotion than stationary periods. Additionally, during locomotion, the distribution of firing rates was less skewed ($\gamma = 1.15$ vs. 1.45 during stationary trials), with a decrease in low and an increase in medium firing rates (KS test, $p < 10^{-6}$). This pattern was also observed in the population of dLGN neurons, where firing rates were consistently higher for trials with locomotion compared to trials when the

animal was stationary (12.7 vs. 9.7 spikes/s; LMM: $F_{1,194.1} = 15.4$, $p = 0.00012$; **Fig. 5c**). Similar to previous reports using gratings [80, 83], we found that bursting was lower during locomotion than stationary periods (0.045 vs. 0.068; LMM: $F_{1,185.4} = 28.5$, $p = 2.7 \times 10^{-7}$; **Fig. 5d**). Beyond these established measures, using movie clips allowed us to test the effects of locomotion on additional response properties: trials with locomotion were associated with lower sparseness (0.40 vs. 0.47; LMM: $F_{1,181.9} = 22.7$, $p = 3.8 \times 10^{-6}$; **Fig. 5e**) and lower trial-to-trial reliability (0.14 vs. 0.17; LMM: $F_{1,190.0} = 10.1$; $p = 0.0018$; **Fig. 5f**). This locomotion-related decrease of reliability could be related to, but is likely not fully explained by, the increase in eye movements typically associated with running (**Fig. 5-Supplement 1h,i**) [80, 84]. These analyses demonstrate that in dLGN, processing of naturalistic movie clips is robustly modulated by locomotion. Curiously, in all aspects tested, these modulations by locomotion had the same signatures as those of CT feedback: increased firing rates, reduced bursting, and decreased sparseness and trial-to-trial reliability.

Since the effects of CT feedback and locomotion closely resembled each other, and since L6CT neurons themselves are modulated by locomotion [85], are the effects of locomotion on dLGN responses inherited via feedback from cortex? To test this hypothesis, we next focused on only those trials with V1 suppression and repeated the separation according to locomotion (**Fig. 5g–h**). These analyses revealed that effects of locomotion persisted, even if CT feedback was suppressed (**Fig. 5i–l**; firing rate: 9.7 vs. 7.5 spikes/s; LMM: $F_{1,183.2} = 18.1$, $p = 3.3 \times 10^{-5}$; burst ratio: 0.084 vs. 0.12 spikes/s; LMM: $F_{1,193.1} = 28.3$, $p = 2.8 \times 10^{-7}$; sparseness: 0.47 vs. 0.56; LMM: $F_{1,179.5} = 54.7$, $p = 5.1 \times 10^{-12}$; reliability: 0.14 vs. 0.18; LMM: $F_{1,187.5} = 22.0$, $p = 5.3 \times 10^{-6}$).

Finally, to test more directly the relationship between effects of behavioral state and CT feedback, we compared CT feedback and running-related modulations on a neuron-by-neuron basis. First, we hypothesized that if effects of locomotion on dLGN responses were inherited from primary visual cortex, such effects should vanish during V1 suppression (**Fig. 6a$_0$**). However, consistent with our observations above (**Fig. 5i–l**), even during V1 suppression, running-related modulations were significantly different from 0 (firing rate run modulation index (RMI): 0.18 ± 0.06; burst ratio: -0.17 ± 0.12; sparseness: -0.12 ± 0.04; reliability: -0.11 ± 0.08; **Fig. 6a$_{1-4}$**). In fact, the degree of running modulation was correlated between feedback and suppression conditions (firing rate: slope of 0.51 ± 0.12; burst ratio: slope of 0.38 ± 0.2; sparseness: slope of 0.44 ± 0.14; reliability: slope of 0.50 ± 0.15; **Fig. 6a$_{1-4}$**). Interestingly, for firing rates and burst ratios, locomotion effects were slightly stronger, on average, with CT feedback intact compared to V1 suppression (firing rate RMI: 0.23 vs. 0.20; LMM: $F_{1,168.3} = 4.3$, $p = 0.04$, **Fig. 6a$_1$**; burst ratio RMI: -0.25 vs. -0.17; LMM: $F_{1,154.7} = 6.3$, $p = 0.013$, **Fig. 6a$_2$**), indicating that these two modulatory influences likely

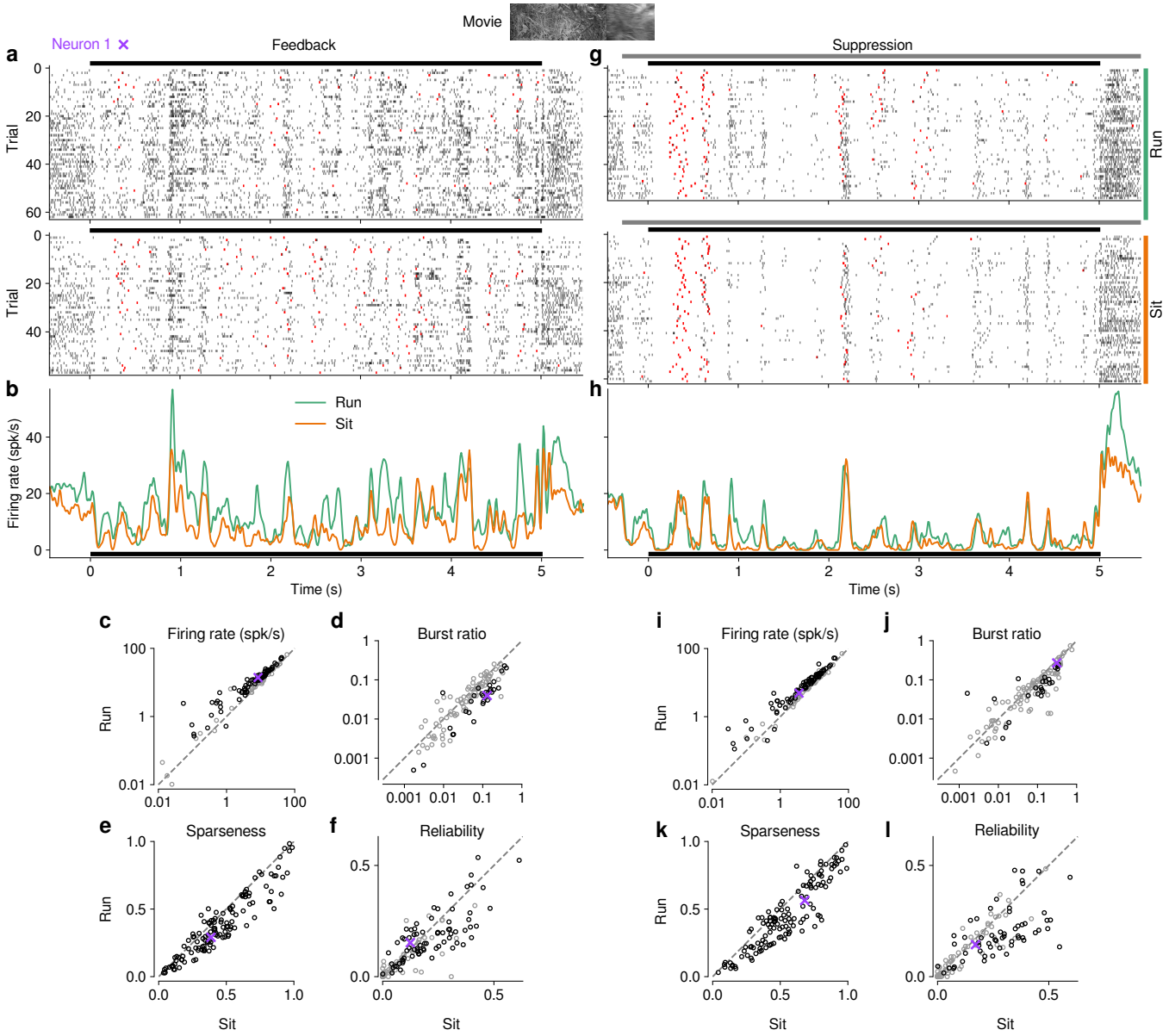

Figure 5 Effects of locomotion on dLGN responses resemble those of CT feedback, but persist even during V1 suppression.

(**a**) Spike raster of example neuron 1 (same as **Fig. 1d**) in response to a naturalistic movie clip during locomotion and stationary trials with CT feedback intact. *Top*: trials with run speed > 1 cm/s; *bottom*: trials with run speed < 0.25 cm/s, both for at least > 50% of each trial. *Red*: burst spikes. (**b**) Corresponding PSTHs. *Green*: locomotion, *orange*: stationary; *black bar*: duration of movie clip. (**c–f**) Comparison of firing rates (c), burst ratio (d), sparseness (e), and trial-to-trial reliability (f) during locomotion and stationary trials. Black markers in (c,d,f) correspond to individually significant observations (Welch's t-test). (**g–l**) Same as (a–f), for locomotion and stationary trials during V1 suppression. See also **Fig. 5-Supplement 1**.

interact.

We next tested the hypothesis that CT feedback might have a stronger impact during active behavioral states than during quiescence. Indeed, it has previously been shown that during brain states associated with anesthesia, the responsiveness of feedback circuits is particularly reduced [30, 56, 57]. One might therefore predict that during quiescence, if feedback circuits were already completely disengaged, we should not be able to observe further effects of V1 suppression (**Fig. 6**$\mathbf{b}_0$). This was clearly not the case, because CT feedback effects were correlated across behavioral states (firing rate: slope of 0.72 ± 0.10; burst ratio: slope of 0.34 ± 0.15; sparseness: slope of 0.85 ± 0.12; reliability: slope of 0.43 ± 0.14; **Fig. 6**$\mathbf{b}_{1-4}$). In addition, and similar to the slightly stronger RMIs during feedback, we discovered a locomotion-dependent CT feedback effect for firing rates and burst ratios. CT feedback effects were slightly stronger, on average, during locomotion than during quiescence (firing rate FMI: 0.18 vs. 0.15; LMM: $F_{1,172.8} = 3.5$, $p = 0.065$; **Fig. 6**$\mathbf{b}_1$; burst ratio FMI: -0.27 vs. -0.19; LMM: $F_{1,166.9} = 6.8$, $p = 0.0097$; **Fig. 6**$\mathbf{b}_2$). This subtle interaction between behavioral state and CT feedback effects might relate to a previous finding, where careful dissection of brain states by depth of anesthesia had already suggested that the effects of transient cortical inactivation on dLGN responses were more evident during lighter anesthesia, i.e., during desynchronized cortical activity [43]. Our ability to observe effects of V1 suppression in dLGN while the animal was stationary suggests that CT feedback circuits are engaged even under conditions of behavioral quiescence and underscores that effects of CT feedback and behavioral state are largely independent.

Finally, if modulations by CT feedback and behavioral state exploited the same circuitry, neurons experiencing strong modulation by V1 suppression should also be strongly affected by locomotion (**Fig. 6**$\mathbf{c}_0$). Contrary to this prediction, we found that effects of CT feedback (FMI) and behavioral state (RMI) were uncorrelated (firing rate: slope of 0.054 ± 0.13; burst ratio: slope of -0.11 ± 0.13; sparseness: slope of -0.053 ± 0.21; reliability: slope of -0.095 ± 0.12; **Fig. 6**$\mathbf{c}_{1-4}$). Together, these comparisons demonstrate that effects of behavioral state associated with locomotion and effects of CT feedback are largely independent.

Discussion

In this study, we used naturalistic movies to reveal that corticothalamic feedback can have substantial and consistent effects on dLGN responses. First, we show that V1 suppression reduces time-varying dLGN firing rates, and leads to increases in bursting, sparseness and trial-to-trial reliability. While changes of time-varying responses to movies were generally well predicted via a divisive reduction in response gain, a simple threshold-linear model could not capture the full spectrum of V1 suppression effects, in particular the nonlinearities

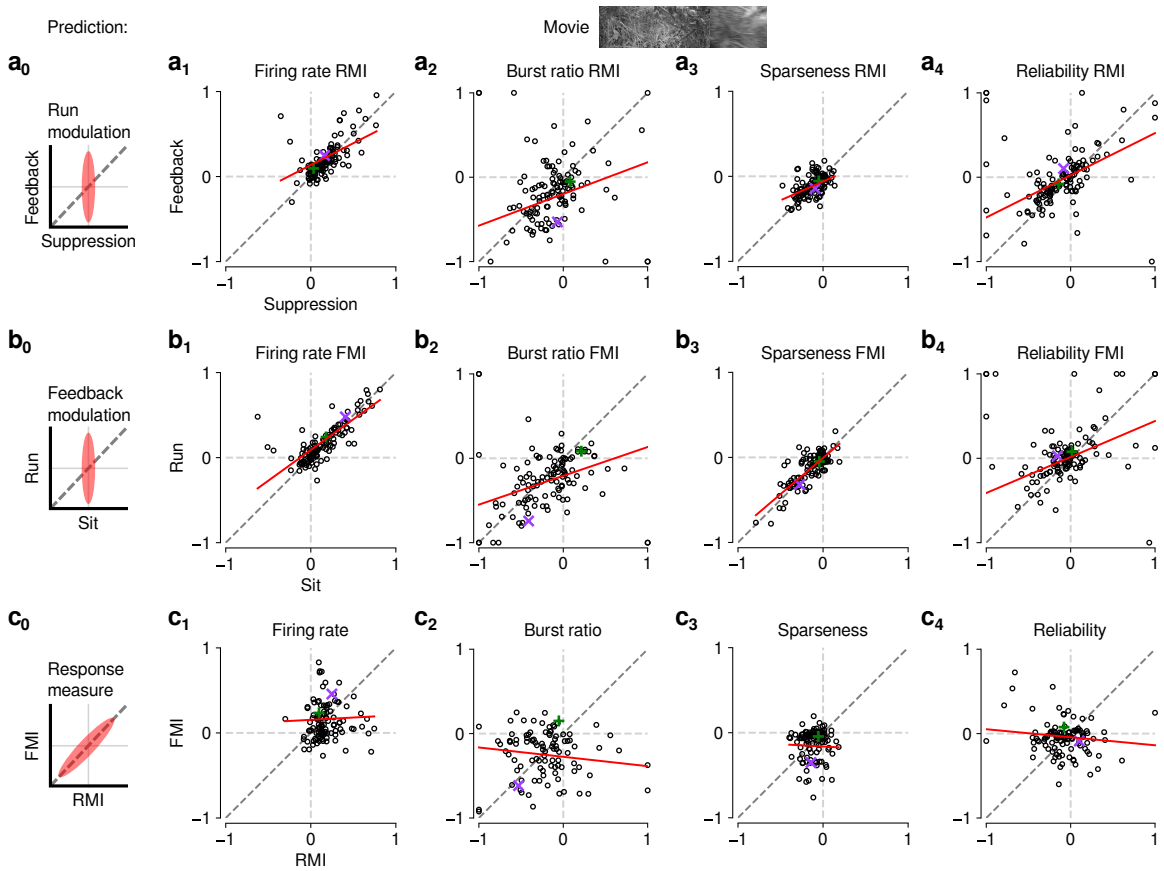

Figure 6 The effects of CT feedback and locomotion on movie responses are largely independent. (**a**$_0$–**c**$_0$) Predicted relationships between modulation indices and response measures in different conditions, assuming dependence in the effects of CT feedback and locomotion. (**a**) Comparison of modulation by running (RMI) during CT feedback intact and V1 suppression for firing rates (a$_1$), burst ratio (a$_2$), sparseness (a$_3$), and reliability (a$_4$). Running effects were quantified with a run modulation index (RMI), where RMI = (running − sitting)/(running + sitting). (**b**) Comparison of modulation by CT feedback (FMI) during locomotion and stationary periods for firing rates (b$_1$), burst ratio (b$_2$), sparseness (b$_3$), and reliability (b$_4$). (**c**) Comparison of modulation by feedback (FMI) and modulation by running (RMI) for firing rates (c$_1$), burst ratio (c$_2$), sparseness (c$_3$), and reliability (c$_4$). *Red*: LMM fit. *Green, purple*: example neurons from **Fig. 2a,b**.

arising from burst spiking. Second, we demonstrate that effects of V1 suppression on firing rate were more consistent and therefore stronger overall for naturalistic movies than for gratings, potentially related to the differential engagement of CT feedback as a function of stimulus context. Third, we show that CT feedback effects on dLGN activity closely resemble effects of behavioral state, as assessed by locomotion. We demonstrate, however, that the effects of V1 suppression on firing rate, bursting, sparseness and reliability are largely independent of modulations by behavioral state, and importantly, that effects of locomotion persist even when V1 activity is suppressed. Together, these findings demonstrate that behavioral modulations of dLGN activity are not simply inherited from cortex. Overall, our findings highlight that dLGN activity can be reliably modulated by two extra-retinal sources – cortical feedback and locomotion – which exert their influences via largely separate routes.

To manipulate CT feedback, we chose a global V1 suppression approach based on optogenetic activation of ChR2 expressed in local PV+ inhibitory interneurons [41, 46–48, 86]. ChR2-based activation of local PV+ inhibitory interneurons results in reliable, continuous, and strong suppression of V1 L6 CT neurons, compared to alternative optogenetic approaches involving direct photosuppression of L6 CT neurons using archaerhodopsin and halorhodopsin [25, 41]. These light-driven pumps pose challenges in terms of light power requirements, temporal decay of sensitivity, and effects on intracellular ion homeostasis [62, 86]. While silencing by excitation of inhibitory interneurons can exploit the robust effects of GABA-mediated inhibition in cortical circuits, it comes with a limitation in specificity. In addition to the direct L6 → thalamus circuit, indirect, polysynaptic effects might be exerted via alternative routes. One example is L5 corticofugal pyramidal cells projecting to the superior colliculus (SC), where tectogeniculate neurons in the superficial layers provide retinotopically organized, driving inputs to the dorsolateral shell region of the dLGN [87]. To address this lack of specificity, in control experiments, we replaced photoactivation of PV+ neurons with direct, selective suppression of V1 Ntsr1+ neurons, which overlap by at least 90% with L6 CT pyramidal cells [63, 64]. Since photosuppression via the novel light-gated chloride channel stGtACR2 [62] did not alter any of our conclusions regarding the effects of CT feedback on dLGN responses, we assume that the effects of V1 suppression to a large degree reflect the specific impact of the L6 CT circuit. L6 CT neurons, however, have an intracortical axon collateral making privileged connections with a translaminar PV+ interneuron subtype in L6 [63, 88], which in turn strongly regulates the gain of the entire V1 column [41, 63, 88]. Since suppression of L6 CT neurons increases the gain in V1 [41], and since this is the opposite of the global effects of V1 suppression via PV+ activation, it is unlikely that the observed modulations of dLGN are largely driven by alternative circuits. Nevertheless, decisively ruling out alternative circuits would require the selective suppression

of L6 CT axon terminals at the thalamic target.

Cortical layer 6 is well known for its especially high diversity of neuronal cell types [16]. Even within the population of L6 CT pyramidal cells there is heterogeneity, with at least 2 subtypes defined by morphology [88–90], 3 subtypes defined by electrophysiology and morphology [90], and 4 major subtypes defined by transcriptomics [89, 90]. Whether these subtypes mediate different aspects of feedback modulations is currently unknown. In the visual system of primates and carnivores, CT feedback circuits seem to be organized into distinct streams [91–93] whose functional organization mimics that of the feedforward streams. Whether the known subtypes in mice can convey independent, stream-specific information is currently unknown, partly because already at the level of feedforward processing, the notion of streams in mouse dLGN is a matter of ongoing debate [94, 94–97], and response properties are diverse [67, 68, 98]. Our own assessment of CT feedback effects revealed few systematic differences for various dLGN cell-type classifications. Such an absence of differences, however, is not surprising, because our manipulation approaches nonspecifically suppressed all L6 CT neuron subtypes. Once genetic targeting of L6 CT subtypes is possible [99, 100], it will be important to test the stream-specificity of CT feedback in the mouse.

Our analyses of the time-varying firing rates in response to naturalistic movies revealed that V1 suppression results in a robust decrease of geniculate response gain. Divisive CT feedback effects have also been previously reported for contrast response functions of parvocellular dLGN neurons in anesthetized macaques [42]. Such divisive gain modulations were commonly thought to arise from shunting inhibition, as opposed to hyperpolarizing inhibition. From simulations, however, it has become clear that in the suprathreshold regime, the effect of shunting synapses is also subtractive [101], even if voltage-dependent inhibitory conductances are considered [102]. Instead, a crucial element to produce gain modulations seems to be changes in the level of synaptically driven V_m fluctuations, often called "synaptic noise" [103–105]. Indeed, *in vivo* V1 recordings suggest that the combined impact of changes in V_m fluctuations, input resistance, and depolarization is needed to produce gain changes [106]. These cellular properties are altered by both feedback [105] and neuromodulation [107], not only in cortex [108] but also in the corticothalamic system [109]. Here, "synaptic noise" together with varying degrees of T-type channel recruitment has been shown to change the slope of the input-output function and alter the temporal filtering characteristics of thalamic relay cells [109, 110]. Thus, by providing variable synaptic input and affecting membrane depolarization, CT feedback might be in a prime position to dynamically tune the gain of the thalamic relay; elucidating the underlying cellular mechanisms will be an important step in the future.

In addition to potentially contributing to the observed gain modulations, "synaptic noise" from CT feedback may also help explain the less precise and less reliable dLGN responses we observed when feedback was left intact. Specifically, V1 neurons are known to exhibit about double the trial-to-trial variability of simultaneously recorded dLGN neurons [111], and eliminating variable cortical input might reveal the even greater reliability of feed-forward retinal inputs [111].

Our analyses of movie and grating response characteristics showed that V1 suppression robustly and consistently biased geniculate activity towards burst firing mode. Burst firing mode occurs when dLGN neurons undergo sustained ($\geq$ 100 ms) hyperpolarization [65], which allows for the de-inactivation of low-threshold T-type calcium channels abundant in thalamus [112]. Previous intracellular recordings in cat dLGN have revealed that cortical ablation can hyperpolarize the resting membrane potential of dLGN relay cells by $\sim$ 9 mV, enough to push them into burst-firing mode [113]. Conversely, direct optogenetic activation of L6 CT neurons in primary somatosensory cortex has been shown to decrease burst mode firing [114]. In burst firing mode, reminiscent of the effects we observed during V1 suppression, dLGN spontaneous activity is low [65], stimulus-evoked responses show phase-advance [75, 115] and high trial-to-trial reliability [115]. The increase in trial-to-trial response reliability we observed during V1 suppression might therefore be explained not only by the removal of a more variable input as mentioned above [111], but also by a shift towards burst mode, where retinogeniculate communication efficacy is elevated [116].

Theories about the function of thalamic firing modes can also provide a useful framework for interpreting the effects of CT feedback we observed here, in particular since the greater precision and trial-to-trial reliability of responses during V1 suppression might be unexpected at first glance. Thalamic burst mode is often linked with "inattentive states", where the sudden appearance or change of a visual stimulus from non-preferred to preferred RF contents [117–119] can reliably trigger a thalamic burst. Bursting is associated with high signal-to-noise, well-suited for stimulus detection [65, 120]. In addition, thalamic burst mode is known to augment the efficacy of retinal input to drive spiking in dLGN [116], and increases the probability of relay between thalamus and cortex, because bursts drive large postsynaptic potentials [121]. This in turn might lead to depolarizing CT feedback, switching the thalamus to tonic mode and allowing more faithful, linear relay of information with a higher dynamic range, better suited for encoding of more finely graded details [65, 109]. Sherman has termed this process a "wake-up-call" for cortex [65, 117], which could represent a neural implementation of bottom-up attention in dLGN [122]. To understand if CT feedback is indeed recruited for detailed perceptual analyses, an essential next step would be to measure the activity of L6 CT neurons under behaviorally relevant conditions. Interestingly, in the

auditory system, activation of L6 CT feedback has been shown to influence sound perception, with enhancements of sound detection or discrimination behavior, depending on the relative timing between CT spiking and stimulus onset [123]. Beyond having broad impact on coding regimes and transmission, bursting in thalamus is also known to have specific computational properties, such as efficiently encoding high- and low-frequency information in parallel [124].

So far, most studies using naturalistic stimuli to probe dLGN responses have been performed in anesthetized animals and have not considered CT feedback [117–119, 125–127]. Similarly, most studies investigating the impact of CT feedback have relied on artificial stimuli [25, 34, 41, 44]. Combining both manipulations to directly compare the effects of CT feedback during naturalistic movies and gratings, we found evidence that CT feedback modulates firing rates at the geniculate level in a stimulus-dependent fashion. For artificial stimuli, such as gratings and bars, it has long been known that CT feedback can enhance dLGN surround suppression by increasing responses to small stimuli and reducing responses to large stimuli [31–35, 37, 39, 77, 78]. Such CT feedback mediated enhancement of surround suppression might result from recruitment of a more narrow direct excitatory and a wider indirect inhibitory CT feedback component according to grating size [78], with the balance shifting more towards direct excitation for small gratings and more towards indirect inhibition for large gratings. Size, however, is likely not the only determinant of relative recruitment of CT feedback circuits: for instance, V1 ablation or pharmacological suppression in anesthetized cats leads to more prominent reductions of dLGN surround suppression for iso- vs. cross-oriented gratings [33, 55], suggesting an additional role of stimulus context. For naturalistic stimuli with complex context, measurements in area V1 have already demonstrated that surround suppression is generally lower than for iso-oriented gratings, and is flexibly invoked depending on the specific statistics in the RF center and surround [79]. The differential effect of CT feedback on dLGN firing rates for full-screen naturalistic movies and iso-oriented gratings observed in our study might therefore be parsimoniously explained by differences in the relative strength of direct excitatory and indirect inhibitory CT feedback. It would be of prime interest to measure, in future experiments, size tuning curves with and without CT feedback using different stimuli, such as naturalistic movies, iso- and cross-oriented gratings. Given our results, we predict that CT feedback would affect firing rate responses to full-screen cross-oriented gratings more similarly to full-screen naturalistic movies than would iso-oriented gratings.

By measuring the effects of V1 suppression during different behavioral states, and by measuring locomotion effects with and without CT feedback, we found that locomotion and CT feedback had similar effects on dLGN responses, but operated via largely separate circuits. The independence of modulations by CT feedback and behavioral state is remarkable:

neuromodulation accompanying locomotion also affects cortical layer 6, which receives dense cholinergic afferents from basal forebrain [128], and mouse V1 L6 CT neurons increase action potential firing in slice recordings upon bath application of ACh [129]. Potentially related, many V1 L6 CT neurons themselves increase activity during locomotion or arousal [85, 130]. While it is therefore unclear why such modulations of V1 L6 CT neurons only contribute relatively little to the dLGN locomotion effects, our result is similar to recent findings in superior colliculus (SC), where locomotion-related response modulations were also independent of V1 feedback [131]. If not inherited from CT feedback [see also 132, 133], which alternative circuits could mediate the effects of locomotion in dLGN [80–82]? Locomotion is accompanied by arousal [134], which in turn involves various neuromodulatory influences [reviewed in 135]. For instance, norepinephrine from the locus coeruleus (LC) and acetylcholine (ACh) from the midbrain are known to act directly on the thalamus [reviewed in 136, 137] and could drive some of the arousal-related depolarizing effects on firing rate independent of cortical feedback, for instance by blocking a long-lasting Ca^{2+}-dependent K^{+} current [138]. In addition, electrical stimulation of the LC [139] and the parabrachial region (PBR) [140] within the mesencephalic locomotor region (MLR), and direct application of noradrenergic [141] and cholinergic [137, 142] agonists within dLGN, are sufficient to reduce thalamic burst mode firing. Finally, at least part of the locomotion effects in dLGN might also be related to modulations of retinal output [131, 143]. Indeed, two-photon calcium imaging of retinal ganglion cell boutons in dLGN [143] and SC [131] revealed that their activity can be modulated by locomotion, albeit with an overall suppressive effect. In future studies, it will be key to further dissect the contributions of retinal, cortical and potentially collicular modulations, and the different neuromodulatory sources of behavioral state-related modulations in thalamic targets.

Acknowledgments

This research was supported by the German Research Foundation (DFG) SFB870 TP19 (LB), DFG BU 1808/5-1 (LB), DFG SFB 1233, Robust Vision: Inference Principles and Neural Mechanisms, TP 13, project number: 276693517 (LB), and by an add-on fellowship of the Joachim Herz Stiftung (GB). We thank D. Metzler for discussions regarding the multi-level modeling, M. Sotgia for lab management and support with animal handling and histology, S. Schörnich for IT support, and B. Grothe for providing excellent research infrastructure.

Materials and Methods

All procedures complied with the European Communities Council Directive 2010/63/EC and the German Law for Protection of Animals, and were approved by local authorities, following appropriate ethics review.

Surgical procedures

Experiments were carried out in 6 adult PV-Cre mice (median age at first recording session: 23.5 weeks; B6;129P2-Pvalb$^{\text{tm1(cre)Arbr}}$/J; Jackson Laboratory) and 3 adult Ntsr1-Cre mice (median age: 29.4 weeks; B6.FVB(Cg)-Tg(Ntsr1-cre)GN220Gsat/Mmcd; MMRRC) of either sex. Thirty minutes prior to the surgical procedure, mice were injected with an analgesic (Metamizole, 200 mg/kg, sc, MSD Animal Health, Brussels, Belgium). To induce anesthesia, animals were placed in an induction chamber and exposed to isoflurane (5% in oxygen, CP-Pharma, Burgdorf, Germany). After induction of anesthesia, mice were fixated in a stereotaxic frame (Drill & Microinjection Robot, Neurostar, Tuebingen, Germany) and the isoflurane level was lowered (0.5%–2% in oxygen), such that a stable level of anesthesia could be achieved as judged by the absence of a pedal reflex. Throughout the procedure, the eyes were covered with an eye ointment (Bepanthen, Bayer, Leverkusen, Germany) and a closed loop temperature control system (ATC 1000, WPI Germany, Berlin, Germany) ensured that the animal's body temperature was maintained at 37° C. At the beginning of the surgical procedure, an additional analgesic was administered (Buprenorphine, 0.1 mg/kg, sc, Bayer, Leverkusen, Germany) and the animal's head was shaved and thoroughly disinfected using idodine solution (Braun, Melsungen, Germany). Before performing a scalp incision along the midline, a local analgesic was delivered (Lidocaine hydrochloride, sc, bela-pharm, Vechta, Germany). The skin covering the skull was partially removed and cleaned from tissue residues with a drop of H_2O_2 (3%, AppliChem, Darmstadt, Germany). Using four reference points (bregma, lambda, and two points 2 mm to the left and to the right of the midline respectively), the animal's head was positioned into a skull-flat configuration. The exposed skull was covered with OptiBond FL primer and adhesive (Kerr dental, Rastatt, Germany) omitting three locations: V1 (AP: -2.8 mm, ML: -2.5 mm), dLGN (AP: -2.3 mm, ML: -2 mm), and a position roughly 1.5 mm anterior and 1 mm to the right of bregma, designated for a miniature reference screw (00-96 X 1/16 stainless steel screws, Bilaney) soldered to a custom-made connector pin. 2 μL of the adeno-associated viral vector rAAV9/1.EF1a.DIO.hChR2(H134R)-eYFP.WPRE.hGH (Addgene, #20298-AAV9) was dyed with 0.3 μL fast green (Sigma-Aldrich, St. Louis, USA). After performing a small craniotomy over V1, in PV-Cre mice a total of ~ 0.5 μL of this mixture was injected across the entire depth of cortex (0.05 μL injected every 100 μm, starting at 1000 μm and ending at

100 μm below the brain surface), using a glass pipette mounted on a Hamilton syringe (SYR 10 μL 1701 RN no NDL, Hamilton, Bonaduz, Switzerland). In V1 of Ntsr1-Cre mice, we injected 0.35 μL of stGtACR2 (pAAV_hSyn1-SIO-stGtACR2-FusionRed, Addgene, #105677; 0.05 μL injected every 100 μm, starting at 1000 μm and ending at 500 μm below the brain surface). A custom-made lightweight stainless steel head bar was positioned over the posterior part of the skull such that the round opening in the bar was centered on V1/dLGN. The head bar was attached with dental cement (Ivoclar Vivadent, Ellwangen, Germany) to the primer/adhesive. The opening was later filled with the silicone elastomer sealant Kwik-Cast (WPI Germany, Berlin, Germany). At the end of the procedure, an antibiotic ointment (Imex, Merz Pharmaceuticals, Frankfurt, Germany) or iodine-based ointment (Braunodivon, 10%, B. Braun, Melsungen, Germany) was applied to the edges of the wound and a long-term analgesic (Meloxicam, 2 mg/kg, sc, Böhringer Ingelheim, Ingelheim, Germany) was administered and for 3 consecutive days. For at least 5 days post-surgery, the animal's health status was assessed via a score sheet. After at least 1 week of recovery, animals were gradually habituated to the experimental setup by first handling them and then simulating the experimental procedure. To allow for virus expression, neural recordings started no sooner than 3 weeks after injection. On the day prior to the first day of recording, mice were fully anesthetized using the same procedures as described for the initial surgery, and a craniotomy (ca. 1.5 mm^2) was performed over dLGN and V1 and re-sealed with Kwik-Cast (WPI Germany, Berlin, Germany). As long as the animals did not show signs of discomfort, the long-term analgesic Metacam was administered only once at the end of surgery, to avoid any confounding effect on experimental results. Recordings were performed daily and continued for as long as the quality of the electrophysiological signals remained high.

Electrophysiological recordings, optogenetic suppression of V1, perfusion

Head-fixed mice were placed on an air-cushioned Styrofoam ball, which allowed the animal to freely move. Two optical computer mice interfaced with a microcontroller (Arduino Duemilanove) sampled ball movements at 90 Hz. To record eye position and pupil size, the animal's eye was illuminated with infrared light and monitored using a zoom lens (Navitar Zoom 6000) coupled with a camera (Guppy AVT camera; frame rate 50 Hz, Allied Vision, Exton, USA). Extracellular signals were recorded at 30 kHz (Blackrock microsystems). For each recording session, the silicon plug sealing the craniotomy was removed. For V1 recordings, a 32 or 64 channel silicon probe (Neuronexus, A1x32-5mm-25-177, A1x32Edge-5mm-20-177-A32 or A1x64-Poly2-6mm-23s-160) was lowered into the brain to a median depth of 1025 μm. For dLGN recordings, a 32 channel linear silicon probe (Neuronexus A1x32Edge-5mm-20-177-A32) was lowered to a depth of $\sim$ 2300–3611 μm below the brain surface. We

judged recording sites to be located in dLGN based on the characteristic progression of RFs from upper to lower visual field along the electrode shank [67] (**Fig. 1-Supplement 1b**), the presence of responses strongly modulated at the temporal frequency of the drifting gratings (F1 response), and the preference of responses to high temporal frequencies [67, 144]. For *post hoc* histological reconstruction of the recording site, the electrode was stained with DiI (Invitrogen, Carlsbad, USA) for one of the final recording sessions.

For photostimulation of V1 PV+ inhibitory interneurons, an optic fiber (910 μm diameter, Thorlabs, Newton, USA) was coupled to a light-emitting diode (LED, center wavelength 470 nm, M470F1, Thorlabs, Newton, USA; or center wavelength 465 nm, LEDC2_465/635_SMA, Doric Lenses, Quebec, Canada) and positioned with a micromanipulator less than 1 mm above the exposed surface of V1. A black metal foil surrounding the tip of the head bar holder prevented the photostimulation light from reaching the animal's eyes. To ensure that the photostimulation was effective, the first recording session for each mouse was carried out in V1. Only if the exposure to light reliably induced suppression of V1 activity was the animal used for subsequent dLGN recordings. For gratings, photostimulation started either 0.1 s before stimulus onset and ended 0.1 s after stimulus offset (2 experiments), or photostimulation started 0.3 s before stimulus onset and ended 0.2 s after stimulus offset (11 experiments), or photostimulation started 0.3 s before stimulus onset and ended 0.45 s after stimulus offset (12 experiments). For movie clips, photostimulation started either 0.1 s before stimulus onset and ended 0.1 s after stimulus offset (2 experiments), or photostimulation started 0.3 s before stimulus onset and ended 0.45 s after stimulus offset (45 experiments). LED light intensity was adjusted on a daily basis to evoke reliable effects (median intensity: 13.66 mW/mm^2 for activating ChR2 in PV-Cre mice, and 10.84 mW/mm^2 for activating stGtACR2 in Ntsr1-Cre mice, as measured at the tip of the optic fiber). Since the tip of the fiber never directly touched the surface of the brain, and since the clarity of the surface of the brain varied (generally decreasing every day following the craniotomy), the light intensity delivered even to superficial layers of V1 was inevitably lower. Importantly, changes in dLGN firing rates induced by V1 suppression (FMI, see below) did not differ, on average, from those induced by behavioral state (RMI, see below) (firing rate: FMI 0.20 vs. RMI 0.15, LMM: $F_{1,145.7} = 3.02$, $p = 0.08$; burst ratio: FMI -0.27 vs. RMI -0.28, $F_{1,124.0} = 0.002$, $p = 0.97$; sparseness: FMI -0.12 vs. RMI -0.14, $F_{1,144.9} = 1.03$, $p = 0.31$; reliability: FMI -0.084 vs. -0.037, $F_{1,183.0} = 1.96$, $p = 0.16$; **Fig. 6c**), indicating that optogenetic stimulation effects were not outside the physiological range.

After the final recording session, mice were first administered an analgesic (Metamizole, 200 mg/kg, sc, MSD Animal Health, Brussels, Belgium) and following a 30 min latency period were transcardially perfused under deep anesthesia using a cocktail of Medetomidin

(Domitor, 0.5 mg/kg, Vetoquinol, Ismaning, Germany), Midazolam (Climasol, 5 mg/kg, Ratiopharm, Ulm, Germany) and Fentanyl (Fentadon, 0.05 mg/kg, Dechra Veterinary Products Deutschland, Aulendorf, Germany) (ip). A few animals, which were treated according to a different license, were anesthetized with sodium pentobarbital (Narcoren, 400 mg/kg, ip, Böhringer Ingelheim, Ingelheim, Germany). Perfusion was first done with Ringer's lactate solution followed by 4% paraformaldehyde (PFA) in 0.2 M sodium phosphate buffer (PBS).

Histology

To verify recording site and virus expression, we performed histological analyses. Brains were removed, postfixed in PFA for 24 h, and then rinsed with and stored in PBS at 4° C. Slices (40 μm) were cut using a vibrotome (Leica VT1200 S, Leica, Wetzlar, Germany), mounted on glass slides with Vectashield DAPI (Vector Laboratories, Burlingame, USA), and coverslipped. A fluorescent microscope (BX61, Olympus, Tokyo, Japan) was used to inspect slices for the presence of yellow fluorescent protein (eYFP) and DiI. Recorded images were processed using FIJI [145, 146].

Visual stimulation

Visual stimuli were presented on a liquid crystal display (LCD) monitor (Samsung SyncMaster 2233RZ, 47×29 cm, 1680×1050 resolution at 60 Hz, mean luminance 50 cd/m^2) positioned at a distance of 25 cm from the animal's right eye (spanning $\sim$ 108×66°, small angle approximation) using custom written software (EXPO, https://sites.google.com/a/nyu.edu/expo/home). The display was gamma-corrected for the presentation of artificial stimuli, but not for movies (see below).

To measure receptive fields (RFs), we mapped the ON and OFF subfields with a sparse noise stimulus. The stimulus consisted of nonoverlapping white and black squares on a square grid, each flashed for 200 ms. For dLGN recordings, the square grid spanned 60° on a side, while individual squares spanned 5° on a side. For a single experiment the vertical extent was reduced to 50°. For subsequent choices of stimuli, RF positions and other tuning preferences were determined online after each experiment based on multiunit activity, i.e. high-pass filtered signals crossing a threshold of 4.5 to 6.5 SD.

We measured single unit orientation preference by presenting full-screen, full-contrast drifting sinusoidal gratings of either 12 (23 experiments) or 8 (2 experiments) different, pseudo-randomly interleaved orientations (30° or 45° steps). For dLGN recordings, spatial frequency was either 0.02 cyc/° (17 experiments) or 0.04 cyc/° (8 experiments) and temporal frequency was either 2 Hz (2 experiments) or 4 Hz (23 experiments). One blank condition (i.e., mean luminance gray screen) was included to allow measurements of spontaneous activity. The stimulus duration was either 2 s (23 experiments) or 5 s (2 experiments), with

an interstimulus interval (ISI) of 2.4 s (21 experiments) or 1.25 s (2 experiments). For two Ntsr1-Cre experiments, ISIs varied and were either 0.58 s or 1.09 s.

For laminar localization of neurons recorded in V1, we presented a full-screen, contrast-reversing checkerboard at 100% contrast, with a spatial frequency of either 0.01 cyc/° (2 experiments) or 0.02 cyc/° (5 experiments) and a temporal frequency of 0.5 cyc/s.

Movies were acquired using a hand-held consumer-grade digital camera (Canon PowerShot SD200) at a resolution of 320×240 pixels and 60 frames/s. Movies were filmed close to the ground in a variety of wooded or grassy locations in Vancouver, BC, and contained little to no forward/backward optic flow, but did contain simulated gaze shifts (up to 275°/s), generated by manual camera movements (for example movies, see **Fig. 1-Video 1** and **Fig. 1-Video 2**). Focus was kept within 2 m and exposure settings were set to automatic. The horizontal angle subtended by the camera lens was 51.6°. No display gamma correction was used while presenting movies, since consumer-grade digital cameras are already gamma corrected for consumer displays [147]. For presentation, movies were cut into 5 s clips and converted from color to grayscale. Movie clips were presented full-screen with an ISI of 1.25 s (43 experiments). For two Ntsr1-Cre experiments, ISIs varied and were either 0.58 s or 1.08 s. white noise: Different clips were presented in pseudorandom order,

Spike sorting

To obtain single unit activity from extracellular recordings, we used the open source, Matlab-based, automated spike sorting toolbox Kilosort [148]. Resulting clusters were manually refined using Spyke [149], a Python application that allows the selection of channels and time ranges around clustered spikes for realignment, as well as representation in 3D space using dimension reduction (multichannel PCA, ICA, and/or spike time). In 3D, clusters were then further split via a gradient-ascent based clustering algorithm (GAC) [150]. Exhaustive pairwise comparisons of similar clusters allowed the merger of potentially over-clustered units. For subsequent analyses, we inspected autocorrelograms and mean voltage traces, and only considered units that displayed a clear refractory period and a distinct spike waveshape. All further analyses were carried out using the DataJoint framework [151] with custom-written code in Python.

Response characterization

We used current source density (CSD) analysis for recordings in area V1 to determine the laminar position of electrode contacts. To obtain the LFP data we first down-sampled the signal to 1 kHz before applying a bandpass filter (4–90 Hz, 2nd-order Butterworth filter). We computed the CSD from the second spatial derivative of the local field potentials [152], and assigned the base of layer 4 to the contact that was closest to the earliest CSD polarity

inversion. The remaining contacts were assigned to supragranular, granular and infragranular layers, assuming a thickness of ~ 1 mm for mouse visual cortex [153].

In recordings targeting dLGN, we used the envelope of multi-unit spiking activity (MUAe) [154] to determine RF progression (**Fig. 1-Supplement 1b**). Briefly, we full-wave rectified the high-pass filtered signals (cutoff frequency: 300 Hz, 4th-order non-causal Butterworth filter) before performing common average referencing by subtracting the median voltage across all channels in order to eliminate potential artifacts (e.g. movement artifacts). We then applied a low-pass filter (cutoff frequency: 500 Hz, Butterworth filter) and down-sampled the signal to 2 kHz. Recording sessions for which RFs did not show the retinotopic progression typical of dLGN (**Fig. 1-Supplement 1b**) [67] were excluded from further analysis.

Each unit's peristimulus time histogram (PSTH, i.e., the response averaged over trials) was calculated by convolving a Gaussian of width $2\sigma = 20$ ms with the spike train collapsed across all trials, separately for each condition.

We defined bursts according to [75], which required a silent period of at least 100 ms before the first spike in a burst, followed by a second spike with an interspike interval < 4 ms. Any subsequent spikes with preceding interspike intervals < 4 ms were also considered to be part of the burst. All other spikes were regarded as tonic. We computed a burst ratio (the number of burst spikes divided by the total number of spikes) and compared this ratio in conditions with CT feedback intact vs. V1 suppression or during locomotion vs. stationary conditions. PSTHs for burst spikes were calculated by only considering spikes that were part of bursts before collapsing across trials and convolving with the Gaussian kernel (see above). PSTHs for non-burst spikes were calculated in an analogous way.

To quantify the effect of V1 suppression on various response properties, we defined the feedback modulation index (FMI) as

$$\text{FMI} = \frac{\text{feedback} - \text{suppression}}{\text{feedback} + \text{suppression}} \tag{1}$$

Characterization of responses to naturalistic movie clips

Signal to noise ratio (SNR) was calculated according to [155] by

$$\text{SNR} = \frac{Var[\langle C_r \rangle]_t}{\langle Var[C]_t \rangle_r} \tag{2}$$

where C is the T by R response matrix (time samples by stimulus repetitions) and $\langle\rangle_x$ and $\text{Var}[]_x$ denote the mean and variance across the indicated dimension, respectively. If all trials were identical such that the mean response was a perfect representative of the response, SNR

would equal 1.

The sparseness S of a PSTH was calculated according to [60] by

$$S = \left(1 - \frac{\left(\sum_{i=1}^{n} r_i/n\right)^2}{\sum_{i=1}^{n} r_i^2/n}\right)\left(\frac{1}{1-1/n}\right) \tag{3}$$

where $r_i \geq 0$ is the signal value in the ith time bin, and n is the number of time bins. Sparseness ranges from 0 to 1, with 0 corresponding to a uniform signal, and 1 corresponding to a signal with all of its energy in a single time bin.

Response reliability was quantified according to [61] as the mean pairwise correlation of all trial pairs of a unit's single trial responses. Single trial responses were computed by counting spikes in 20 ms, overlapping time bins at 1 ms resolution. Pearson's correlation was calculated between all possible pairs of trials, and then averaged across trials per condition.

To detect response peaks in trial raster plots and measure their widths, clustering of spike times collapsed across trials was performed using the gradient ascent clustering (GAC) algorithm [150], with a characteristic neighborhood size of 20 ms. Spike time clusters containing less than 5 spikes were discarded. The center of each detected cluster of spike times was matched to the nearest peak in the PSTH. A threshold of $\theta = b + 3$ Hz was applied to the matching PSTH peak, where $b = 2\,\mathrm{median}(x)$ is the baseline of each PSTH x. Peaks in the PSTH that fell below θ were discarded, and all others were kept as valid peaks. Peak widths were measured as the temporal separation of the middle 68% (16th to 84th percentile) of spike times within each cluster.

To determine whether V1 suppression changes dLGN responses in a divisive or subtractive manner, we fit a threshold-linear model using repeated random subsampling cross-validation. To this end, we first selected a random set of 50% of the trials for each condition for fitting to the timepoint-by-timepoint responses a threshold linear model given by $R_{supp} = s\,R_{fb} + b$, where $R_{supp} > 0$, with s representing the slope and b the offset. Fitting was done using non-linear least squares (`scipy.optimize.curve_fit`). Throughout **Fig. 2**, we report the resulting x-intercept as the threshold. We evaluated goodness of fit (R^2) for the other 50% of trials not used for fitting. We repeated this procedure 1000 times and considered threshold and slope as significant if the central 95% of their distribution did not include 0 and 1, respectively.

Characterization of responses to drifting gratings

For display of spike rasters (**Fig. 3**), trials were sorted by condition. We computed orientation tuning curves by fitting a sum of two Gaussians of the same width with peaks 180° apart:

$$R(\theta) = R_0 + R_p e^{-\frac{(\theta-\theta_p)^2}{2\sigma^2}} + R_n e^{-\frac{(\theta-\theta_p+180)^2}{2\sigma^2}} \tag{4}$$

In this expression, θ is stimulus orientation (0–360°). The function has five parameters: preferred orientation θ_p, tuning width σ, baseline response (offset independent of orientation) R_0, response at the preferred orientation R_p, and response at the null orientation R_n.

Orientation selectivity was quantified according to [41, 156] as

$$\text{OSI} = \frac{\sqrt{(\sum R_k \sin(2\theta_k))^2 + (\sum R_k \cos(2\theta_k))^2}}{\sum R_k} \tag{5}$$

where R_k is the response to the kth direction given by θ_k. We determined OSI for each unit during both feedback and suppression conditions.

We computed the first harmonic of the response R from the spike trains according to [74] to obtain the amplitude and phase of the best-fitting sinusoid, which has the same temporal frequency as the stimulus. For each trial, we calculated

$$R = (1/D) \sum_k \cos(2\pi f t_k) + i \sin(2\pi f t_k) \tag{6}$$

where D is the stimulus duration, f is the temporal frequency of the stimulus, and the t_k are the times of the individual spikes. We excluded the first cycle to avoid contamination by the onset response. For (**Fig. 3g**), we calculated average amplitude F_1 by obtaining the absolute value of the complex number R on each trial, before averaging across trials, to avoid potential confounds due to differences in response phase across conditions. For the comparison of response phase, we focused on the orientation which elicited the maximal cycle average response across both feedback and suppression conditions.

Cell typing

Units were classified as suppressed by contrast (SbC) or not suppressed by contrast (non-SbC) by comparing their mean firing rates during full-screen drifting grating presentation to their mean firing rates during blank-screen presentation. Units were classified as SbC if they were visually responsive to gratings (see below) and had a median z-scored response across orientation conditions of ≤ -3 during at least one grating experiment. Otherwise, units were classified as non-SbC. SbC units seem to constitute a sizeable fraction in our dataset,

which is similar to our previous results [68], where SbC was also found to be among the overrepresented retinal ganglion cell (RGC) types providing input to dLGN.

To identify electrode channels within the putative shell/core of the dLGN, we concentrated on the RF progression as assessed with MUAe maps that were constructed using sparse noise experiments. Because RF progression is mainly along elevation, amplitudes of MUAe for each channel were collapsed across azimuth and then range normalized. Channels with normalized amplitudes higher than an empirically set threshold (0.4) were considered part of dLGN. Non-detected channels located between detected channels were added. We considered neurons to be located in putative dLGN shell if their mean spike waveform had the largest amplitude on one of the uppermost 20% of electrode channels classified as falling within dLGN.

Direction selectivity index (DSI, [157]) was calculated for each unit as

$$\mathrm{DSI} = \frac{R_p - R_n}{R_p + R_n + 2R_0} \tag{7}$$

where R_p and R_n are the firing rates in the preferred and null directions, respectively, extracted from tuning curves fit to drifting grating responses (see above), and R_0 is baseline firing rate independent of orientation.

The RF distance from the center of the screen was calculated for each unit by finding the position of the MUAe RF for the channel on which the unit's mean spike waveform had the largest amplitude.

Exclusion criteria

Neurons with mean evoked firing rates < 0.01 spikes/s were excluded from further analysis. For movie clips, only neurons with SNR ≥ 0.015 in at least one of the conditions in an experiment were considered. Of this population, 2 neurons were excluded from the analysis of the parameters returned by the threshold linear model, because their R^2 was < 0. For gratings, we converted firing rates in response to each orientation to z-scores relative to responses to the mean luminance gray screen. We only considered visually responsive neurons, with an absolute z-scored response ≥ 2.5 to at least 1 orientation. For the analysis of response phase, we only considered neurons with a peak of the cycle average response of at least 10 Hz in both feedback and suppression conditions, and an F_1/F_0 ratio of at least 0.25.

Locomotion

We used the Euclidean norm of three perpendicular components of ball velocity (roll, pitch and yaw) to compute animal running speed. For the analysis of neural responses as a

function of behavioral state, locomotion trials were defined as those for which speed exceeded 1 cm/s for at least 50% of the stimulus presentation, and stationary trials as those for which speed fell below 0.25 cm/s for at least 50% of the stimulus presentation. To quantify the effect of running vs. sitting on various response properties, the run modulation index (RMI) was defined as

$$\mathrm{RMI} = \frac{\mathrm{running} - \mathrm{sitting}}{\mathrm{running} + \mathrm{sitting}} \tag{8}$$

Although other measures of behavioral state such as pupil size indicate that the animal may be in an active/ aroused state outside of periods of locomotion [134, 158, 159], we have chosen to use locomotion to categorize trials for several reasons. Firstly, it is clear from the aforementioned studies that the largest changes in neural activity (at the level of the visual cortex) occur as a function of locomotion. Secondly, because pupil size and locomotion fluctuations are highly correlated [80], using one measure or the other would likely result in a similar separation of trials. Finally, our naturalistic movie stimuli contain dynamic changes in luminance, which drive changes in pupil size that would act as a confound to behavioral state classification.

Eye Tracking

The stimulus viewing eye was filmed using an infrared camera under infrared LED illumination. Pupil position was extracted from the videos using a custom, semi-automated algorithm. Briefly, each video frame was equalized using an adaptive bi-histogram equalization procedure, and then smoothed using median and bilateral filters. The center of the pupil was detected by taking the darkest point in a convolution of the filtered image with a black square. Next, the peaks of the image gradient along lines extending radially from the center point were used to define the pupil contour. Lastly, an ellipse was fit to the contour, and the center of this ellipse was taken as the position of the pupil. A similar procedure was used to extract the position of the corneal reflection (CR) of the LED illumination. Eye blinks were automatically detected and the immediately adjacent data points were excluded. Adjustable algorithm parameters were set manually for each experiment. Output pupil position time-courses were lightly smoothed, and unreliable segments were automatically removed according to *a priori* criteria. Finally, the CR position was subtracted from the pupil position to eliminate translational eye movements, and pupil displacement in degrees relative to the baseline (median) position was determined by

$$\theta = 2\,\frac{\arcsin(d/2)}{r} \tag{9}$$

where d is the distance between the pupil and the baseline position, and $r = 1.25$ mm is the radius of the eye [160]. Angular displacement was computed separately for x and y directions.

Eye position standard deviation was computed by first taking the standard deviation of the horizontal eye position at each time point across trials, and then averaging over the 5 s during which the visual stimulus was presented. We focused on horizontal eye position because horizontal and vertical eye movements tend to occur in tandem under head-fixed conditions, and the horizontal position variance is larger [161], thus serving as a better proxy for variance in 2D. For each experiment, trials were sorted either by the presence of optogenetic suppression of CT feedback (**Fig. 1-Supplement 2h**), or by the behavioral state of the animal as described above (**Fig. 5-Supplement 1h**). The eye position standard deviation FMI and RMI (**Fig. 1-Supplement 2i** and **Fig. 5-Supplement 1i**) were calculated in the same manner as for the neural response properties.

Statistical methods

To assess statistical significance, we fitted and examined multilevel linear models [162]. Such models take into account the hierarchical structure present in our data (i.e., neurons nested in experiments, experiments nested in recording sessions, recordings sessions nested in animals), and eliminate the detrimental effect of structural dependencies on the likelihood of Type I errors (false positive reports) [163]. By considering the nested structure of the data, multilevel models also eliminate the need for "pre-selecting" data sets, such as one out of several experiments repeatedly performed on the same neurons. Whenever we have several experiments per neuron, we include all of them, and also show them in the scatter plots ("observations"). We provide the sample size for each analysis in **Table 1**. In fitting the models, we accounted for repeated measures by including random effects for animals, recording sessions, experiments, and neurons. We fit these models in R [164], using the *lme4* package [165]. We estimated F-values, their degrees of freedom, and the corresponding p-values using the Satterthwaite approximation [166] implemented by the *lmertest* package [167]. Throughout, uncertainty in estimated regression slopes is represented as $slope \pm x$, where x is $2\times$ the estimated standard error of the slope.

Data and code availability

Data and source code used to generate the figures in the manuscript will be made available on Dryad.

	Observations	**Neurons**	**Mice**
Figure 1f–i	124	65	6
Figure 2e–h	119	63	6
Figure 3c–e,g	68	44	4
Figure 3f	36	28	4
Figure 3h–i	50	35	3
Figure 4a–b	39	39	4
Figure 5c–e	130	66	6
Figure 5f,i–l	129	66	6
Figure $6a_1$,a_3	126	64	6
Figure $6a_2$	109	58	6
Figure $6a_4$	111	63	6
Figure $6b_1$,c_3	123	63	6
Figure $6b_2$	110	58	6
Figure $6b_4$	109	62	6
Figure $6c_1$,c_3,c_4	109	59	6
Figure $6c_2$	101	56	6
Figure 1S2a	124	65	6
Figure 1S2b,g	108	57	6
Figure 1S2c	117	63	6
Figure 1S2d–f	118	64	6
Figure 1S2h	22	n/a	6
Figure 1S2i	124	64	6
Figure 1S3a,c	39	39	4
Figure 1S3b	63	63	6
Figure 1S3d	54	54	6
Figure 1S3e	64	64	6
Figure 1S3f,h	38	38	4
Figure 1S3g	62	62	6
Figure 1S3i	53	53	6
Figure 1S3j	63	63	6
Figure 1S4e–h	64	59	3
Figure 1S4l,n	110	73	3
Figure 1S4m	98	71	3
Figure 3S1a,c,e	44	44	4
Figure 3S1b	63	63	6

Figure 3S1d	36	36	4
Figure 3S1f,h,j	42	42	4
Figure 3S1g	40	40	4
Figure 3S1i	35	35	4
Figure 4S1a	65	42	4
Figure 4S1b	43	43	4
Figure 4S1c–d, g, j	124	65	6
Figure 4S1e	36	36	3
Figure 4S1f	29	29	3
Figure 4S1h–i,k	68	44	4
Figure 4S1l	66	43	4
Figure 5S1a	130	66	6
Figure 5S1b,g	102	56	6
Figure 5S1c	107	57	6
Figure 5S1d,f	129	65	6
Figure 5S1e,i	125	65	6
Figure 5S1h	30	n/a	6

Table 1 Breakdown of sample sizes (N) for the analyses of neural data. See text for details.

Author contributions

Conceptualization, L.B. and M.A.S; Methodology, M.A.S., D.C.; Software, M.A.S., S.K., G.B., D.C., Y.B., X.L.; Formal Analysis, S.K.; Investigation, M.A.S., Y.B.; Data Curation, M.A.S., G.B., D.C., L.B.; Writing – Original Draft, L.B., G.B.; Writing – Review & Editing, L.B., S.K., M.A.S., G.B., D.C.; Visualization, M.A.S., G.B., S.K.; Supervision, L.B.; Project Administration, L.B.; Funding Acquisition, L.B.

Competing interests

The authors declare no competing interests.

References

1. Lien, A. D. & Scanziani, M. Cortical direction selectivity emerges at convergence of thalamic synapses. *Nature* **558**, 80–86 (2018).

2. Hubel, D. H. & Wiesel, T. N. Receptive fields, binocular interaction and functional architecture in the cat's visual cortex. *J. Physiol.* **160**, 106–154 (1962).

3. Chance, F. S., Nelson, S. B. & Abbott, L. F. Complex cells as cortically amplified simple cells. *Nat. Neurosci.* **2**, 277–282 (1999).

4. Riesenhuber, M. & Poggio, T. Hierarchical models of object recognition in cortex. *Nat. Neurosci.* **2**, 1019–1025 (1999).

5. Riesenhuber, M. & Poggio, T. Models of object recognition. *Nat. Neurosci.* **3**, 1199–1204 (2000).

6. DiCarlo, J. J., Zoccolan, D. & Rust, N. C. How Does the Brain Solve Visual Object Recognition? *Neuron* **73**, 415–434 (2012).

7. Squire, R. F., Noudoost, B., Schafer, R. J. & Moore, T. Prefrontal contributions to visual selective attention. *Annu. Rev. Neurosci.* **36**, 451–466 (2013).

8. Roelfsema, P. R. & de Lange, F. P. Early Visual Cortex as a Multiscale Cognitive Blackboard. *Annu. Rev. Vis. Sci.* **2**, 131–151 (2016).

9. Bastos, A. M. *et al.* Canonical microcircuits for predictive coding. *Neuron* **76**, 695–711 (2012).

10. Lamme, V. A. F. & Roelfsema, P. R. The distinct modes of vision offered by feedforward and recurrent processing. *Trends Neurosci.* **23**, 571–579 (2000).

11. Takahashi, N., Oertner, T. G., Hegemann, P. & Larkum, M. E. Active cortical dendrites modulate perception. *Science* **354**, 1587–1590 (2016).

12. Larkum, M. A cellular mechanism for cortical associations: An organizing principle for the cerebral cortex. *Trends Neurosci.* **36**, 141–151 (2013).

13. Heeger, D. J. Theory of cortical function. *Proc. Natl. Acad. Sci. U.S.A.* **114**, 1773–1782 (2017).

14. Gilbert, C. D. & Li, W. Top-down influences on visual processing. *Nat. Rev. Neurosci.* **14**, 350–63 (2013).

15. Sherman, S. M. & Guillery, R. W. The role of the thalamus in the flow of information to the cortex. *Philos. Trans. Royal Soc. B* **357**, 1695–708 (2002).

16. Briggs, F. Organizing principles of cortical layer 6. *Front. Neural Circuits* **4**, 3 (2010).

17. Sillito, A. M. & Jones, H. E. Corticothalamic interactions in the transfer of visual information. *Philos. Trans. Royal Soc. B* **357**, 1739–1752 (2002).

18. Vélez-Fort, M. *et al.* The stimulus selectivity and connectivity of layer six principal cells reveals cortical microcircuits underlying visual processing. *Neuron* **83**, 1431–43 (2014).

19. Stoelzel, C. R., Bereshpolova, Y., Alonso, J.-M. & Swadlow, H. A. Axonal Conduction Delays, Brain State, and Corticogeniculate Communication. *J. Neurosci.* **37**, 6342–6358 (2017).

20. Crandall, S. R., Patrick, S. L., Cruikshank, S. J. & Connors, B. W. Infrabarrels Are Layer 6 Circuit Modules in the Barrel Cortex that Link Long-Range Inputs and Outputs. *Cell Rep.* **21**, 3065–3078 (2017).

21. Oberlaender, M. *et al.* Cell Type–Specific Three-Dimensional Structure of Thalamocortical Circuits in a Column of Rat Vibrissal Cortex. *Cereb. Cortex* **22**, 2375–2391 (2012).

22. Swadlow, H. A. Efferent neurons and suspected interneurons in S-1 vibrissa cortex of the awake rabbit: Receptive fields and axonal properties. *J. Neurophysiol.* **62**, 288–308 (1989).

23. Pauzin, F. P. & Krieger, P. A Corticothalamic Circuit for Refining Tactile Encoding. *Cell Rep.* **23**, 1314–1325 (2018).

24. Andermann, M. L. *et al.* Chronic cellular imaging of entire cortical columns in awake mice using microprisms. *Neuron* **80**, 900–13 (2013).

25. Denman, D. J. & Contreras, D. Complex effects on in vivo visual responses by specific projections from mouse cortical layer 6 to dorsal lateral geniculate nucleus. *J. Neurosci.* **35**, 9265–9280 (2015).

26. Sherman, S. M. & Guillery, R. W. On the actions that one nerve cell can have on another: Distinguishing “drivers” from “modulators”. *Proc. Natl. Acad. Sci. U.S.A.* **95**, 7121–7126 (1998).

27. Godwin, D. W. *et al.* Ultrastructural Localization Suggests that Retinal and Cortical Inputs Access Different Metabotropic Glutamate Receptors in the Lateral Geniculate Nucleus. *J. Neurosci.* **16**, 8181–8192 (1996).

28. Usrey, W. M. & Sherman, S. M. Corticofugal circuits: Communication lines from the cortex to the rest of the brain. *J. Comp. Neurol.* **527**, 640–650 (2018).

29. Briggs, F. & Usrey, W. M. Emerging views of corticothalamic function. *Curr. Opin. Neurobiol.* **18**, 403–407 (2008).

30. Briggs, F. & Usrey, W. M. Corticogeniculate feedback and visual processing in the primate. *J. Physiol.* **589**, 33–40 (2011).

31. Wang, W., Andolina, I. M., Lu, Y., Jones, H. E. & Sillito, A. M. Focal Gain Control of Thalamic Visual Receptive Fields by Layer 6 Corticothalamic Feedback. *Cerebral Cortex* **28**, 267–280 (2018).

32. Andolina, I. M., Jones, H. E. & Sillito, A. M. Effects of cortical feedback on the spatial properties of relay cells in the lateral geniculate nucleus. *J. Neurophysiol.* **109**, 889–899 (2013).

33. Cudeiro, J. & Sillito, A. M. Spatial frequency tuning of orientation-discontinuity-sensitive corticofugal feedback to the cat lateral geniculate nucleus. *J. Physiol.* **490 (Pt 2)**, 481–492 (1996).

34. Murphy, P. C. & Sillito, A. M. Corticofugal feedback influences the generation of length tuning in the visual pathway. *Nature* **329**, 727–729 (1987).

35. Webb, B. S. *et al.* Feedback from V1 and inhibition from beyond the classical receptive field modulates the responses of neurons in the primate lateral geniculate nucleus. *Visual Neurosci.* **19**, 583–592 (2002).

36. Nolt, M. J., Kumbhani, R. D. & Palmer, L. A. Suppression at High Spatial Frequencies in the Lateral Geniculate Nucleus of the Cat. *J. Neurophysiol.* **98**, 1167–1180 (2007).

37. Hasse, J. M. & Briggs, F. Corticogeniculate feedback sharpens the temporal precision and spatial resolution of visual signals in the ferret. *Proc. Natl. Acad. Sci. U.S.A.* **114**, E6222–E6230 (2017).

38. Rivadulla, C., Martínez, L. M., Varela, C. & Cudeiro, J. Completing the corticofugal loop: A visual role for the corticogeniculate type 1 metabotropic glutamate receptor. *J. Neurosci.* **22**, 2956–2962 (2002).

39. Jones, H. E. *et al.* Differential feedback modulation of center and surround mechanisms in parvocellular cells in the visual thalamus. *J. Neurosci.* **32**, 15946–15951 (2012).

40. Andolina, I. M., Jones, H. E., Wang, W. & Sillito, A. M. Corticothalamic feedback enhances stimulus response precision in the visual system. *Proc. Natl. Acad. Sci. U.S.A.* **104**, 1685–1690 (2007).

41. Olsen, S. R., Bortone, D. S., Adesnik, H. & Scanziani, M. Gain control by layer six in cortical circuits of vision. *Nature* **483**, 47–52 (2012).

42. Przybyszewski, A. W., Gaska, J. P., Foote, W. & Pollen, D. A. Striate cortex increases contrast gain of macaque LGN neurons. *Visual Neurosci.* **17**, 485–494 (2000).

43. Wörgötter, F., Eyding, D., Macklis, J. D. & Funke, K. The influence of the corticothalamic projection on responses in thalamus and cortex. *Philos. Trans. Royal Soc. B* **357**, 1823–1834 (2002).

44. Wang, W., Jones, H. E., Andolina, I. M., Salt, T. E. & Sillito, A. M. Functional alignment of feedback effects from visual cortex to thalamus. *Nat. Neurosci.* **9**, 1330–1336 (2006).

45. de Labra, C. *et al.* Changes in Visual Responses in the Feline dLGN: Selective Thalamic Suppression Induced by Transcranial Magnetic Stimulation of V1. *Cereb. Cortex* **17**, 1376–1385 (2007).

46. Li, Y.-T., Ibrahim, L. A., Liu, B.-H., Zhang, L. I. & Tao, H. W. Linear transformation of thalamocortical input by intracortical excitation. *Nat. Neurosci.* **16**, 1324–30 (2013).

47. Lien, A. D. & Scanziani, M. Tuned thalamic excitation is amplified by visual cortical circuits. *Nat. Neurosci.* **16**, 1315–23 (2013).

48. King, J. L., Lowe, M. P., Stover, K. R., Wong, A. A. & Crowder, N. A. Adaptive Processes in Thalamus and Cortex Revealed by Silencing of Primary Visual Cortex during Contrast Adaptation. *Curr. Biol.* **26**, 1295–1300 (2016).

49. Berkes, P., Orbán, G., Lengyel, M. & Fiser, J. Spontaneous Cortical Activity Reveals Hallmarks of an Optimal Internal Model of the Environment. *Science* **331**, 83–87 (2011).

50. Lee, T. S. & Mumford, D. Hierarchical Bayesian inference in the visual cortex. *JOSA A* **20**, 1434–1448 (2003).

51. Rao, R. P. N. & Ballard, D. H. Predictive coding in the visual cortex: A functional interpretation of some extra-classical receptive-field effects. *Nat. Neurosci.* **2**, 79–87 (1999).

52. Clark, A. Whatever next? Predictive brains, situated agents, and the future of cognitive science. *Behav. Brain. Sci.* **36**, 181–204 (2013).

53. Gulyás, B., Lagae, L., Eysel, U. & Orban, G. A. Corticofugal feedback influences the responses of geniculate neurons to moving stimuli. *Exp. Brain Res.* **79**, 441–446 (1990).

54. Poltoratski, S., Maier, A., Newton, A. T. & Tong, F. Figure-Ground Modulation in the Human Lateral Geniculate Nucleus Is Distinguishable from Top-Down Attention. *Curr. Biol.* **29**, 2051–2057 (2019).

55. Sillito, A. M., Cudeiro, J. & Murphy, P. C. Orientation sensitive elements in the corticofugal influence on centre-surround interactions in the dorsal lateral geniculate nucleus. *Experimental Brain Research* **93**, 6–16 (1993).

56. Makino, H. & Komiyama, T. Learning enhances the relative impact of top-down processing in the visual cortex. *Nat. Neurosci.* **18**, 1116–1122 (2015).

57. Keller, A. J., Roth, M. M. & Scanziani, M. Feedback generates a second receptive field in neurons of the visual cortex. *Nature* 1–5 (2020).

58. Atallah, B. V., Bruns, W., Carandini, M. & Scanziani, M. Parvalbumin-Expressing Interneurons Linearly Transform Cortical Responses to Visual Stimuli. *Neuron* **73**, 159–170 (2012).

59. Sherman, S. M. Thalamus plays a central role in ongoing cortical functioning. *Nat. Neurosci.* **19**, 533–541 (2016).

60. Vinje, W. E. & Gallant, J. L. Sparse coding and decorrelation in primary visual cortex during natural vision. *Science* **287**, 1273–1276 (2000).

61. Goard, M. & Dan, Y. Basal forebrain activation enhances cortical coding of natural scenes. *Nat. Neurosci.* **12**, 1444–1449 (2009).

62. Mahn, M. *et al.* High-efficiency optogenetic silencing with soma-targeted anion-conducting channelrhodopsins. *Nat. Commun.* **9**, 4125 (2018).

63. Bortone, D. S., Olsen, S. R. & Scanziani, M. Translaminar inhibitory cells recruited by layer 6 corticothalamic neurons suppress visual cortex. *Neuron* **82**, 474–85 (2014).

64. Kim, J., Matney, C. J., Blankenship, A., Hestrin, S. & Brown, S. P. Layer 6 corticothalamic neurons activate a cortical output layer, layer 5a. *Journal of Neuroscience* **34**, 9656–64 (2014).

65. Sherman, S. M. Tonic and burst firing: dual modes of thalamocortical relay. *Trends Neurosci* **24**, 122–126 (2001).

66. Guido, W. & Weyand, T. Burst responses in thalamic relay cells of the awake behaving cat. *Journal of Neurophysiology* **74**, 1782–1786 (1995).

67. Piscopo, D. M., El-Danaf, R. N., Huberman, A. D. & Niell, C. M. Diverse visual features encoded in mouse lateral geniculate nucleus. *J. Neurosci.* **33**, 4642–56 (2013).

68. Román Rosón, M. *et al.* Mouse dLGN Receives Functional Input from a Diverse Population of Retinal Ganglion Cells with Limited Convergence. *Neuron* **102**, 1–15 (2019).

69. Marshel, J. H., Kaye, A. P., Nauhaus, I. & Callaway, E. M. Anterior-posterior direction opponency in the superficial mouse lateral geniculate nucleus. *Neuron* **76**, 713–20 (2012).

70. Cruz-Martín, A. *et al.* A dedicated circuit links direction-selective retinal ganglion cells to the primary visual cortex. *Nature* **507**, 358–61 (2014).

71. Zhao, X., Chen, H., Liu, X. & Cang, J. Orientation-selective responses in the mouse lateral geniculate nucleus. *Journal of Neuroscience* **33**, 12751–63 (2013).

72. Scholl, B., Tan, A. Y. Y., Corey, J. & Priebe, N. J. Emergence of orientation selectivity in the Mammalian visual pathway. *J. Neurosci.* **33**, 10616–24 (2013).

73. Skottun, B. C. *et al.* Classifying simple and complex cells on the basis of response modulation. *Vision Res.* **31**, 1079–1086 (1991).

74. Carandini, M., Heeger, D. J. & Movshon, J. A. Linearity and Normalization in Simple Cells of the Macaque Primary Visual Cortex. *J. Neurosci.* **17**, 8621–8644 (1997).

75. Lu, S. M., Guido, W. & Sherman, S. M. Effects of membrane voltage on receptive field properties of lateral geniculate neurons in the cat: Contributions of the low-threshold Ca2+ conductance. *Journal of Neurophysiology* **68**, 2185–2198 (1992).

76. Grubb, M. S. & Thompson, I. D. Visual Response Properties of Burst and Tonic Firing in the Mouse Dorsal Lateral Geniculate Nucleus. *Journal of Neurophysiology* **93**, 3224–3247 (2005).

77. McClurkin, J. W. & Marrocco, R. T. Visual cortical input alters spatial tuning in monkey lateral geniculate nucleus cells. *The Journal of Physiology* **348**, 135–152 (1984).

78. Born, G. *et al.* Corticothalamic feedback sculpts visual spatial integration in mouse thalamus. *bioRxiv* 2020.05.19.104000 (2021).

79. Coen-Cagli, R., Kohn, A. & Schwartz, O. Flexible gating of contextual influences in natural vision. *Nature Neuroscience* **18**, 1648–1655 (2015).

80. Erisken, S. *et al.* Effects of Locomotion Extend throughout the Mouse Early Visual System. *Curr. Biol.* **24**, 2899–2907 (2014).

81. Aydın, Ç., Couto, J., Giugliano, M., Farrow, K. & Bonin, V. Locomotion modulates specific functional cell types in the mouse visual thalamus. *Nat. Commun.* **9**, 4882 (2018).

82. Williamson, R. S., Hancock, K. E., Shinn-Cunningham, B. G. & Polley, D. B. Locomotion and Task Demands Differentially Modulate Thalamic Audiovisual Processing during Active Search. *Curr. Biol.* **25**, 1885–1891 (2015).

83. Niell, C. M. & Stryker, M. P. Modulation of Visual Responses by Behavioral State in Mouse Visual Cortex. *Neuron* **65**, 472–479 (2010).

84. Bennett, C., Arroyo, S. & Hestrin, S. Subthreshold Mechanisms Underlying State-Dependent Modulation of Visual Responses. *Neuron* **80**, 350–357 (2013).

85. Augustinaite, S. & Kuhn, B. Complementary Ca2+ Activity of Sensory Activated and Suppressed Layer 6 Corticothalamic Neurons Reflects Behavioral State. *Current Biology* (2020).

86. Wiegert, J. S., Mahn, M., Prigge, M., Printz, Y. & Yizhar, O. Silencing Neurons: Tools, Applications, and Experimental Constraints. *Neuron* **95**, 504–529 (2017).

87. Bickford, M. E., Zhou, N., Krahe, T. E., Govindaiah, G. & Guido, W. Retinal and Tectal "Driver-Like" Inputs Converge in the Shell of the Mouse Dorsal Lateral Geniculate Nucleus. *J. Neurosci.* **35**, 10523–10534 (2015).

88. Frandolig, J. E. *et al.* The Synaptic Organization of Layer 6 Circuits Reveals Inhibition as a Major Output of a Neocortical Sublamina. *Cell Reports* **28**, 3131–3143.e5 (2019).

89. Tasic, B. *et al.* Adult mouse cortical cell taxonomy revealed by single cell transcriptomics. *Nature Neuroscience* **19**, 335–346 (2016).

90. Gouwens, N. W. *et al.* Classification of electrophysiological and morphological neuron types in the mouse visual cortex. *Nature Neuroscience* **22**, 1182–1195 (2019).

91. Briggs, F., Kiley, C. W., Callaway, E. M. & Usrey, W. M. Morphological Substrates for Parallel Streams of Corticogeniculate Feedback Originating in Both V1 and V2 of the Macaque Monkey. *Neuron* **90**, 388–399 (2016).

92. Hasse, J. M., Bragg, E. M., Murphy, A. J. & Briggs, F. Morphological heterogeneity among corticogeniculate neurons in ferrets: Quantification and comparison with a previous report in macaque monkeys. *Journal of Comparative Neurology* **527**, 546–557 (2019).

93. Briggs, F. & Usrey, W. M. Parallel Processing in the Corticogeniculate Pathway of the Macaque Monkey. *Neuron* **62**, 135–146 (2009).

94. Chen, C., Bickford, M. E. & Hirsch, J. A. Untangling the Web between Eye and Brain. *Cell* **165**, 20–21 (2016).

95. Denman, D. J. & Contreras, D. On Parallel Streams through the Mouse Dorsal Lateral Geniculate Nucleus. *Frontiers in Neural Circuits* **10** (2016).

96. Morgan, J. L., Berger, D. R., Wetzel, A. W. & Lichtman, J. W. The Fuzzy Logic of Network Connectivity in Mouse Visual Thalamus. *Cell* **165**, 192–206 (2016).

97. Zhuang, J. *et al.* The spatial structure of feedforward information in mouse primary visual cortex. *bioRxiv* 2019.12.24.888156 (2019).

98. Liang, L. *et al.* A Fine-Scale Functional Logic to Convergence from Retina to Thalamus. *Cell* **173**, 1343–1355.e24 (2018).

99. Graybuck, L. T. *et al.* Enhancer viruses for combinatorial cell-subclass-specific labeling. *Neuron* (2021).

100. Mich, J. K. *et al.* Functional enhancer elements drive subclass-selective expression from mouse to primate neocortex. *Cell Reports* **34**, 108754 (2021).

101. Holt, G. R. & Koch, C. Shunting Inhibition Does Not Have a Divisive Effect on Firing Rates. *Neural Computation* **9**, 1001–1013 (1997).

102. Doiron, B., Longtin, A., Berman, N. & Maler, L. Subtractive and Divisive Inhibition: Effect of Voltage-Dependent Inhibitory Conductances and Noise. *Neural Computation* **13**, 227–248 (2001).

103. Hô, N. & Destexhe, A. Synaptic Background Activity Enhances the Responsiveness of Neocortical Pyramidal Neurons. *Journal of Neurophysiology* **84**, 1488–1496 (2000).

104. Shu, Y., Hasenstaub, A., Badoual, M., Bal, T. & McCormick, D. A. Barrages of Synaptic Activity Control the Gain and Sensitivity of Cortical Neurons. *Journal of Neuroscience* **23**, 10388–10401 (2003).

105. Chance, F. S., Abbott, L. F. & Reyes, A. D. Gain Modulation from Background Synaptic Input. *Neuron* **35**, 773–782 (2002).

106. Cardin, J. A., Palmer, L. A. & Contreras, D. Cellular Mechanisms Underlying Stimulus-Dependent Gain Modulation in Primary Visual Cortex Neurons In Vivo. *Neuron* **59**, 150–160 (2008).

107. Disney, A. A., Aoki, C. & Hawken, M. J. Gain Modulation by Nicotine in Macaque V1. *Neuron* **56**, 701–713 (2007).

108. Ferguson, K. A. & Cardin, J. A. Mechanisms underlying gain modulation in the cortex. *Nature Reviews Neuroscience* 1–13 (2020).

109. Béhuret, S., Deleuze, C. & Bal, T. Corticothalamic Synaptic Noise as a Mechanism for Selective Attention in Thalamic Neurons. *Frontiers in Neural Circuits* **9** (2015).

110. Wolfart, J., Debay, D., Le Masson, G., Destexhe, A. & Bal, T. Synaptic background activity controls spike transfer from thalamus to cortex. *Nature Neuroscience* **8**, 1760–1767 (2005).

111. Kara, P., Reinagel, P. & Reid, R. C. Low Response Variability in Simultaneously Recorded Retinal, Thalamic, and Cortical Neurons. *Neuron* **27**, 635–646 (2000).

112. Jahnsen, H. & Llinás, R. Voltage-dependent burst-to-tonic switching of thalamic cell activity: An in vitro study. *Arch. Ital. Biol.* **122**, 73–82 (1984).

113. Dossi, R. C., Nuñez, A. & Steriade, M. Electrophysiology of a slow (0.5-4 Hz) intrinsic oscillation of cat thalamocortical neurones in vivo. *J. Physiol.* **447**, 215–234 (1992).

114. Mease, R. A., Krieger, P. & Groh, A. Cortical control of adaptation and sensory relay mode in the thalamus. *Proc. Natl. Acad. Sci. U.S.A.* **111**, 6798–6803 (2014).

115. Alitto, H. J., Weyand, T. G. & Usrey, W. M. Distinct Properties of Stimulus-Evoked Bursts in the Lateral Geniculate Nucleus. *Journal of Neuroscience* **25**, 514–523 (2005).

116. Alitto, H., Rathbun, D. L., Vandeleest, J. J., Alexander, P. C. & Usrey, W. M. The Augmentation of Retinogeniculate Communication during Thalamic Burst Mode. *J. Neurosci.* **39**, 5697–5710 (2019).

117. Lesica, N. A. & Stanley, G. B. Encoding of Natural Scene Movies by Tonic and Burst Spikes in the Lateral Geniculate Nucleus. *J. Neurosci.* **24**, 10731–10740 (2004).

118. Lesica, N. A. *et al.* Dynamic Encoding of Natural Luminance Sequences by LGN Bursts. *PLoS Biol.* **4** (2006).

119. Wang, X. *et al.* Feedforward Excitation and Inhibition Evoke Dual Modes of Firing in the Cat's Visual Thalamus during Naturalistic Viewing. *Neuron* **55**, 465–478 (2007).

120. Whitmire, C. J., Waiblinger, C., Schwarz, C. & Stanley, G. B. Information Coding through Adaptive Gating of Synchronized Thalamic Bursting. *Cell Reports* **14**, 795–807 (2016).

121. Swadlow, H. A. & Gusev, A. G. The impact of 'bursting' thalamic impulses at a neocortical synapse. *Nature Neuroscience* **4**, 402–408 (2001).

122. Hochstein, S. & Ahissar, M. View from the Top: Hierarchies and Reverse Hierarchies in the Visual System. *Neuron* **36**, 791–804 (2002).

123. Guo, W., Clause, A. R., Barth-Maron, A. & Polley, D. B. A Corticothalamic Circuit for Dynamic Switching between Feature Detection and Discrimination. *Neuron* **95**, 180–194 (2017).

124. Mease, R. A., Kuner, T., Fairhall, A. L. & Groh, A. Multiplexed Spike Coding and Adaptation in the Thalamus. *Cell Rep.* **19**, 1130–1140 (2017).

125. Dan, Y., Atick, J. J. & Reid, R. C. Efficient coding of natural scenes in the lateral geniculate nucleus: experimental test of a computational theory. *J. Neurosci.* **16**, 3351–3362 (1996).

126. Lesica, N. A. *et al.* Adaptation to Stimulus Contrast and Correlations during Natural Visual Stimulation. *Neuron* **55**, 479–491 (2007).

127. Mante, V., Frazor, R. A., Bonin, V., Geisler, W. S. & Carandini, M. Independence of luminance and contrast in natural scenes and in the early visual system. *Nat. Neurosci.* **8**, 1690–1697 (2005).

128. Radnikow, G. & Feldmeyer, D. Layer- and Cell Type-Specific Modulation of Excitatory Neuronal Activity in the Neocortex. *Frontiers in Neuroanatomy* **12** (2018).

129. Sundberg, S. C., Lindström, S. H., Sanchez, G. M. & Granseth, B. Cre-expressing neurons in visual cortex of Ntsr1-Cre GN220 mice are corticothalamic and are depolarized by acetylcholine. *Journal of Comparative Neurology* **526**, 120–132 (2018).

130. Swadlow, H. A. & Weyand, T. G. Corticogeniculate neurons, corticotectal neurons, and suspected interneurons in visual cortex of awake rabbits: Receptive-field properties, axonal properties, and effects of EEG arousal. *Journal of Neurophysiology* **57**, 977–1001 (1987).

131. Schröder, S. *et al.* Arousal Modulates Retinal Output. *Neuron* **107**, 487–495.e9 (2020).

132. Murata, Y. & Colonnese, M. T. Thalamus Controls Development and Expression of Arousal States in Visual Cortex. *J. Neurosci.* **38**, 8772–8786 (2018).

133. Nestvogel, D. B. & McCormick, D. A. Visual Thalamocortical Mechanisms of Waking State Dependent Activity and Alpha Oscillations. *bioRxiv* 2021.04.14.439865 (2021).

134. Vinck, M., Batista-Brito, R., Knoblich, U. & Cardin, J. A. Arousal and Locomotion Make Distinct Contributions to Cortical Activity Patterns and Visual Encoding. *Neuron* **86**, 740–754 (2015).

135. Zagha, E. & McCormick, D. A. Neural control of brain state. *Current Opinion in Neurobiology* **29**, 178–186 (2014).

136. Lee, S.-H. & Dan, Y. Neuromodulation of Brain States. *Neuron* **76**, 209–222 (2012).

137. McCormick, D. A. Neurotransmitter actions in the thalamus and cerebral cortex and their role in neuromodulation of thalamocortical activity. *Progress in Neurobiology* **39**, 337–388 (1992).

138. Sherman, S. M. & Koch, C. The control of retinogeniculate transmission in the mammalian lateral geniculate nucleus. *Experimental Brain Research* **63**, 1–20 (1986).

139. Holdefer, R. N. & Jacobs, B. L. Phasic stimulation of the locus coeruleus: Effects on activity in the lateral geniculate nucleus. *Experimental Brain Research* **100**, 444–452 (1994).

140. Lu, S. M., Guido, W. & Sherman, S. M. The brain-stem parabrachial region controls mode of response to visual stimulation of neurons in the cat's lateral geniculate nucleus. *Visual Neuroscience* **10**, 631–642 (1993).

141. Funke, K., Pape, H. C. & Eysel, U. T. Noradrenergic modulation of retinogeniculate transmission in the cat. *The Journal of Physiology* **463**, 169–191 (1993).

142. Sillito, A. M., Kemp, J. A. & Berardi, N. The cholinergic influence on the function of the cat dorsal lateral geniculate nucleus (dLGN). *Brain Research* **280**, 299–307 (1983).

143. Liang, L. *et al.* Retinal Inputs to the Thalamus Are Selectively Gated by Arousal. *Current Biology* **30**, 3923–3934 (2020).

144. Grubb, M. S. & Thompson, I. D. Quantitative Characterization of Visual Response Properties in the Mouse Dorsal Lateral Geniculate Nucleus. *J. Neurophysiol.* **90**, 3594–3607 (2003).

145. Rueden, C. T. *et al.* ImageJ2: ImageJ for the next generation of scientific image data. *BMC Bioinf.* **18** (2017).

146. Schindelin, J. *et al.* Fiji: An open-source platform for biological-image analysis. *Nat. Methods* **9**, 676–682 (2012).

147. Poynton, C. A. Rehabilitation of gamma. In Rogowitz, B. E. & Pappas, T. N. (eds.) *Human Vision and Electronic Imaging III*, vol. 3299, 232–249 (International Society for Optical Engineering, San Jose, CA, 1998). URL http://www.poynton.com/PDFs/Rehabilitation_of_gamma.pdf.

148. Pachitariu, M., Steinmetz, N. A., Kadir, S. N., Carandini, M. & Harris, K. D. Fast and accurate spike sorting of high-channel count probes with KiloSort. In Lee, D. D., Sugiyama, M., Luxburg, U. V., Guyon, I. & Garnett, R. (eds.) *Advances in Neural Information Processing Systems 29*, 4448–4456 (Curran Associates, Inc., 2016).

149. Spacek, M. A., Blanche, T. J. & Swindale, N. V. Python for large-scale electrophysiology. *Front. Neuroinform.* **2**, 9 (2009). URL http://swindale.ecc.ubc.ca/code.

150. Swindale, N. V. & Spacek, M. A. Spike sorting for polytrodes: a divide and conquer approach. *Front. Syst. Neurosci.* **8**, 6 (2014).

151. Yatsenko, D., Walker, E. Y. & Tolias, A. S. DataJoint: A simpler relational data model. *arXiv* **1807**, 11104 (2018).

152. Mitzdorf, U. Current source-density method and application in cat cerebral cortex: Investigation of evoked potentials and EEG phenomena. *Physiol. Rev.* **65**, 37–100 (1985).

153. Heumann, D., Leuba, G. & Rabinowicz, T. Postnatal development of the mouse cerebral neocortex. II. Quantitative cytoarchitectonics of visual and auditory areas. *J. Hirnforsch.* **18**, 483–500 (1977).

154. van der Togt, C., Spekreijse, H. & Supèr, H. Neural responses in cat visual cortex reflect state changes in correlated activity. *Eur. J. Neurosci.* **22**, 465–475 (2005).

155. Baden, T. *et al.* The functional diversity of retinal ganglion cells in the mouse. *Nature* **529**, 345–350 (2016).

156. Bonhoeffer, T., Kim, D.-S., Malonek, D., Shoham, D. & Grinvald, A. Optical Imaging of the Layout of Functional Domains in Area 17 and Across the Area 17/18 Border in Cat Visual Cortex. *Eur. J. Neurosci.* **7**, 1973–1988 (1995).

157. Niell, C. M. & Stryker, M. P. Highly selective receptive fields in mouse visual cortex. *J Neurosci* **28**, 7520–7536 (2008).

158. Reimer, J. *et al.* Pupil Fluctuations Track Fast Switching of Cortical States during Quiet Wakefulness. *Neuron* **84**, 355–362 (2014).

159. McGinley, M. J., David, S. V. & McCormick, D. A. Cortical Membrane Potential Signature of Optimal States for Sensory Signal Detection. *Neuron* **87**, 179–192 (2015).

160. Remtulla, S. & Hallett, P. A schematic eye for the mouse, and comparisons with the rat. *Vision Res.* **25**, 21–31 (1985).

161. Sakatani, T. & Isa, T. Quantitative analysis of spontaneous saccade-like rapid eye movements in c57bl/6 mice. *Neuroscience research* **58**, 324–331 (2007).

162. Gelman, A. & Hill, J. *Data Analysis Using Regression and Multilevel/Hierarchical Models.* Analytical Methods for Social Research (Cambridge University Press, Cambridge, 2007).

163. Aarts, E., Verhage, M., Veenvliet, J. V., Dolan, C. V. & van der Sluis, S. A solution to dependency: Using multilevel analysis to accommodate nested data. *Nat. Neurosci.* **17**, 491–496 (2014).

164. R Core Team. *R: A Language and Environment for Statistical Computing.* R Foundation for Statistical Computing, Vienna, Austria (2017). URL https://www.R-project.org/.

165. Bates, D., Mächler, M., Bolker, B. & Walker, S. Fitting Linear Mixed-Effects Models Using **lme4**. *J. Stat. Softw.* **67** (2015).

166. Luke, S. G. Evaluating significance in linear mixed-effects models in R. *Behav. Res. Methods* **49**, 1494–1502 (2017).

167. Kuznetsova, A., Brockhoff, P. B. & Christensen, R. H. B. **lmerTest** Package: Tests in Linear Mixed Effects Models. *J. Stat. Softw.* **82** (2017).

Supplementary Information

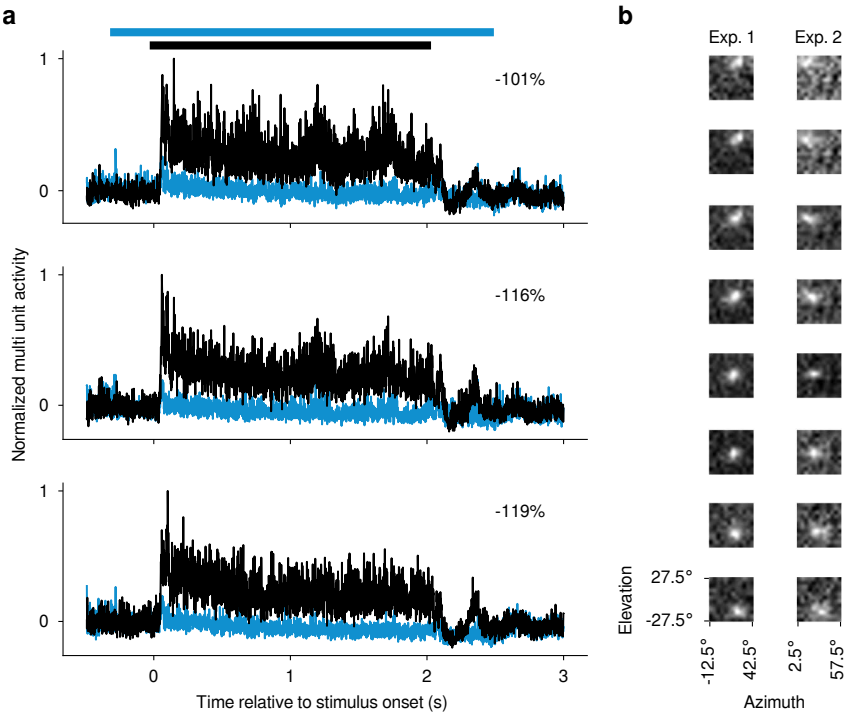

Figure 1-Supplement 1 Confirmation of optogenetic suppression of V1 responses and targeting dLGN for recordings.
(**a**) MUAe responses [154] to 2 s drifting gratings recorded in one experiment for three example channels. All three channels were located, as determined by current source density analysis [152], in the infragranular layers of V1. *Black*: Mean MUAe responses across control trials; *blue*: MUAe responses in trials with optogenetic activation of PV+ inhibitory interneurons. Normalized MUAe was computed by subtracting the mean activity across both conditions in a 200 ms time window prior to light onset before normalizing to the maximum response across the two conditions. Percentages indicate mean reduction in MUAe over the stimulus presentation period. *Black bar*: stimulus period; *blue bar*: photoactivation period. (**b**) MUAe-based RFs for channels located in dLGN during two example RF mapping experiments. Each panel represents one channel, with the top channel being located most dorsally and the bottom channel most ventrally in the dLGN. RFs were computed as the mean response to a change in contrast at a given monitor position in a time window ranging from 50 ms after stimulus onset to 100 ms after stimulus offset. Brighter pixels indicate higher activity. The emerging characteristic pattern with more ventrally located channels representing locations lower in the visual field was used to confirm successful targeting of dLGN.

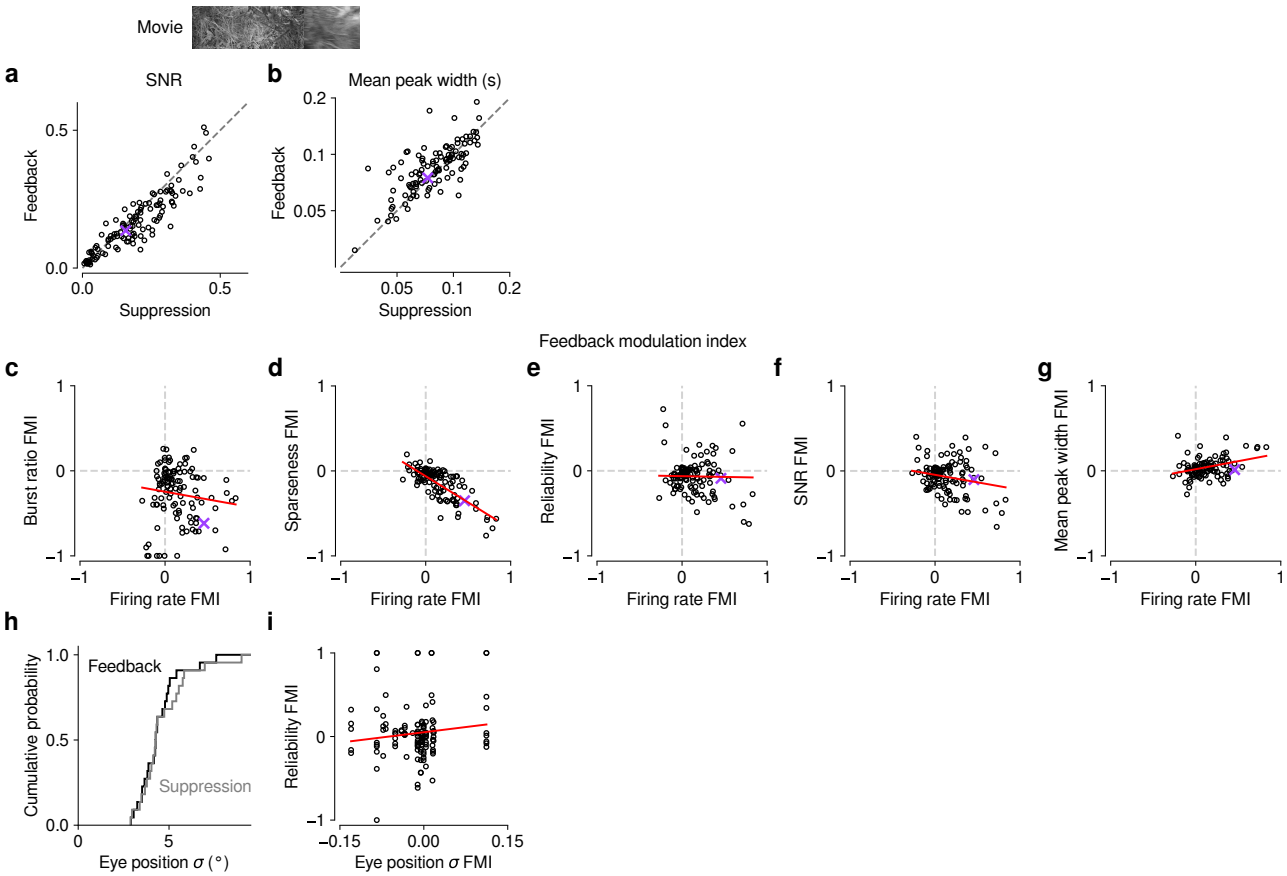

Figure 1-Supplement 2 Effects of CT feedback on additional parameters of responses to naturalistic movies and relationship with firing rate.

(**a,b**) Comparison of CT feedback vs. V1 suppression conditions for PSTH signal-to-noise ratio (SNR) (a) and mean peak width (b). SNR was computed as in [155], and compares the variance of the trial-averaged PSTH across time relative to the single-trial variance across time, averaged across stimulus repeats. If all trials are identical such that the PSTH is a perfect representation of each trial's response, SNR equals 1. The width of PSTH peaks that exceeded a threshold amplitude was measured as the temporal separation of the middle 68% of spikes clustered as part of each peak (see Methods). Narrow peaks are a proxy for high temporal precision of responses. With CT feedback intact, mean SNR was lower (0.15 vs. 0.18, LMM: $F_{1,180.6} = 11.2$, $p = 0.00098$) and mean peak width was higher (0.087 vs. 0.081, LMM: $F_{1,154.15} = 7.0$, $p = 0.0091$). (**c–g**) Relationship between CT feedback effects on firing rate and burst ratio (c), sparseness (d), reliability (e), SNR (f), and mean peak width (g). Feedback effects were quantified with a feedback modulation index (FMI), where FMI = (feedback − suppressed)/(feedback + suppressed). CT feedback-related changes in firing rate can to a large degree account for the changes in sparseness (LMM: slope of -0.62 ± 0.11; (d)). Importantly, for all other measures, there was no systematic relation to the feedback manipulation of firing rates because slopes were either non-significant or close to 0 (burst ratio, LMM: slope of -0.18 ± 0.29; reliability, LMM: -0.018 ± 0.19; SNR, LMM: slope of -0.18 ± 0.18; mean peak width, LMM: slope of 0.19 ± 0.11; estimated slope $\pm$ 2× the estimated standard error). (**h**) Cumulative distribution of variance in eye position with CT feedback intact (*black*) and suppressed (*gray*). Eye position standard deviation was, on average, slightly greater during V1 suppression than during feedback (4.5° vs. 4.3°, LMM: $F_{1,21} = 4.4$, $p = 0.049$, $N = 22$ experiments from 6 mice). (**i**) The strength of CT feedback effects on reliability is unrelated to the strength of feedback effects on eye position (LMM: slope 0.83 ± 1.27). The results from (h) and (i) are inconsistent with the hypothesis that CT feedback effects on trial-to-trial reliability can be explained by changes in eye position variance.

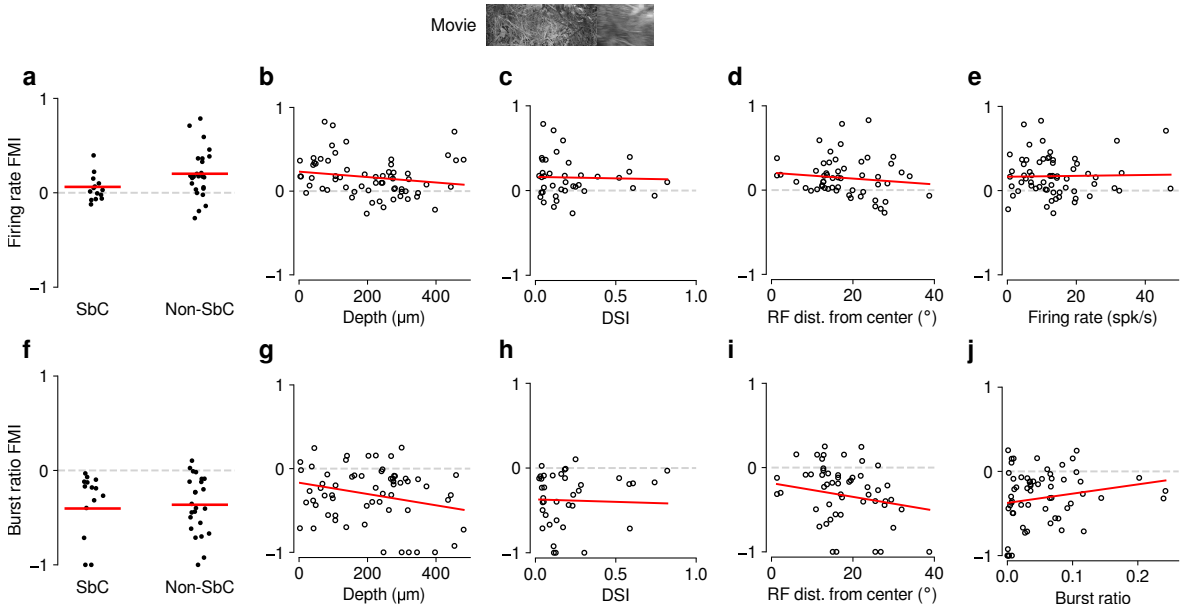

Figure 1-Supplement 3 Feedback effects during movie presentation are largely independent of functional cell type classification.

The dLGN is a non-homogeneous nucleus, consisting of different neuronal cell types [67, 68]. To test if the effect of CT feedback depended on functional cell type, we performed functional cell typing of neurons in various ways. None of the classifications yielded significant results. (**a**) Firing rate FMI distributions during movie presentation, with units classified according to whether or not they were suppressed by contrast (SbC) [67, 68]. Units were defined as SbC if their mean firing rates to uniform equiluminant gray screen were $\geq 3\times$ that of a full-contrast stimulus. CT feedback effects on firing rates tended to be lower for SbC neurons compared to the rest of the population, but not significantly (SbC: 0.062 vs. non-SbC: 0.20; LMM: $F_{1,37.0} = 3.51$, $p = 0.069$). (**b**) Firing rate FMI during movie presentation, plotted against estimated depth of each unit in dLGN (slope -0.00032 ± 0.00046). (**c**) Same as (b), but with units plotted against the direction selectivity index (DSI) [157] of each unit (slope -0.034 ± 0.37). (**d**) Same as (c), but with units plotted against the distance of their RFs from the center of the screen (slope -0.0035 ± 0.0083). We considered distance from center of screen as a proxy for RF coverage by the visual stimuli, which we hypothesized might modulate CT feedback effects through its known effects on spatial integration [78]. (**e**) Same as (d), but with units plotted against their mean firing rate during the feedback intact condition (slope 0.00052 ± 0.006). This indicates that the CT feedback modulation of firing rates does not depend on overall firing rate, i.e. that neurons do not share the same gain factor (see also **Fig. 2e,i**). (**f–j**) Same as (a–e), but for burst ratio (-0.40 (SbC) vs. -0.36 (non-SbC); LMM: $F_{1,30.8} = 0.42$, $p = 0.52$; depth: slope -0.00067 ± 0.0006; DSI: slope -0.057 ± 0.3; RF distance: slope -0.0081 ± 0.01; burst ratio: slope 1.1 ± 1.3). In summary, except for modest trends of differential CT feedback modulations of SbC neurons, we did not find any difference in how feedback affected the various subpopulations. The general similarity of CT feedback effects across classifications might be related to a lack of power (cell-typing in high-dimensional space requires high neuron counts) and to the global suppression approach.

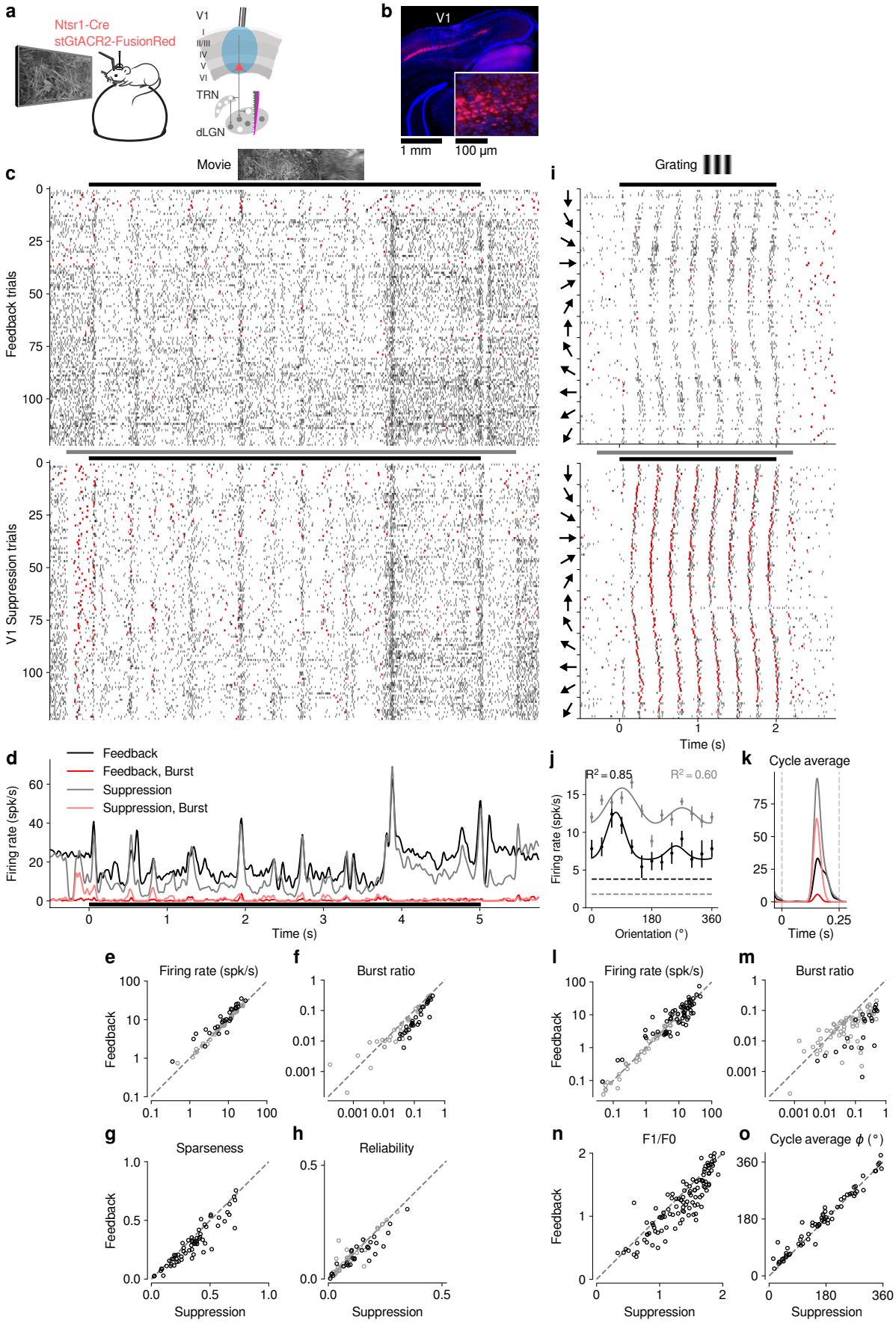
a
Ntsr1-Cre
stGtACR2-FusionRed
V1
I
II/III
IV
V
VI
TRN
dLGN
b
V1
1 mm
100 µm
c
Movie
Feedback trials
V1 Suppression trials
i
Grating
Time (s)
d
Feedback
Feedback, Burst
Suppression
Suppression, Burst
Firing rate (spk/s)
Time (s)
j
R² = 0.85
R² = 0.60
Firing rate (spk/s)
Orientation (°)
k
Cycle average
Time (s)
e
Firing rate (spk/s)
Feedback
f
Burst ratio
g
Sparseness
Suppression
h
Reliability
Suppression
l
Firing rate (spk/s)
Feedback
m
Burst ratio
n
F1/F0
Feedback
Suppression
o
Cycle average ϕ (°)
Suppression

Figure 1-Supplement 4 (**Previous page**) Selective optogenetic suppression of L6 CT feedback in Ntsr1-Cre yielded similar results as global V1 suppression via PV+ activation.
(**a**) Schematic of experimental approach. The chloride-conducting, inhibitory opsin stGtACR2 [62] was conditionally expressed in V1 Ntsr1+ neurons (*red*) using a viral approach. Extracellular silicon electrode recordings were performed in dLGN with and without optogenetic suppression of V1. (**b**) Coronal section of V1 for an example Ntsr1-Cre mouse, showing transduced Ntsr1+ neurons (*magenta*) located in the deep layers of V1. *Blue*: cell nuclei stained with DAPI. *Inset*: magnified view with expression of stGtACR2 largely restricted to somata. (**c**) Movie raster plots during feedback and suppression for an example neuron. (**d**) Corresponding PSTHs. (**e–h**) Comparison of CT feedback vs. suppression conditions for mean firing rate (e), burst ratio (f), temporal sparseness (g), and response reliability (h), all calculated for the duration of the movie clip. Similar to our results for global V1 suppression, CT feedback enhanced firing rates (10.4 (feedback) vs. 9.0 spikes/s (suppression); LMM: $F_{1,68.3} = 9.2$, $p = 0.0034$), reduced bursting (0.083 vs. 0.12; LMM: $F_{1,67.7} = 57.6$, $p = 1.3 \times 10^{-10}$), reduced sparseness (0.31 vs. 0.36; LMM: $F_{1,68.1} = 37.9$, $p = 4.4 \times 10^{-8}$), and reduced trial-to-trial reliability (0.10 vs. 0.11; LMM: $F_{1,66.3} = 5.1$, $p = 0.027$). (**i**) Grating raster plots sorted by orientation, during CT feedback and suppression conditions for a different example neuron. (**j,k**) Corresponding orientation tuning curves and cycle average responses to preferred orientation. (**l–o**) Comparison of feedback vs. suppression conditions for mean firing rate (l), burst ratio (m), F_1/F_0 (n), and cycle average phase ϕ (o). Similar to our results for global V1 suppression, CT feedback had no consistent effect on firing rate (11.10 (feedback) vs. 11.09 spikes/s (suppression); LMM: $F_{1,137.9} = 0.0001$, $p = 0.99$), but reduced bursting (0.04 vs. 0.12; LMM: $F_{1,127.5} = 43.7$, $p = 9.4 \times 10^{-10}$), and reduced F_1/F_0 (1.2 vs. 1.3; LMM: $F_{1,142.9} = 13.0$, $p = 0.00043$). Black symbols in (e,f,h,l,m) indicate individually significant neurons (Welch's t-test).

Figure 1-Video 1 First example 5 s movie clip used for visual stimulation.

Figure 1-Video 2 Second example 5 s movie clip used for visual stimulation.

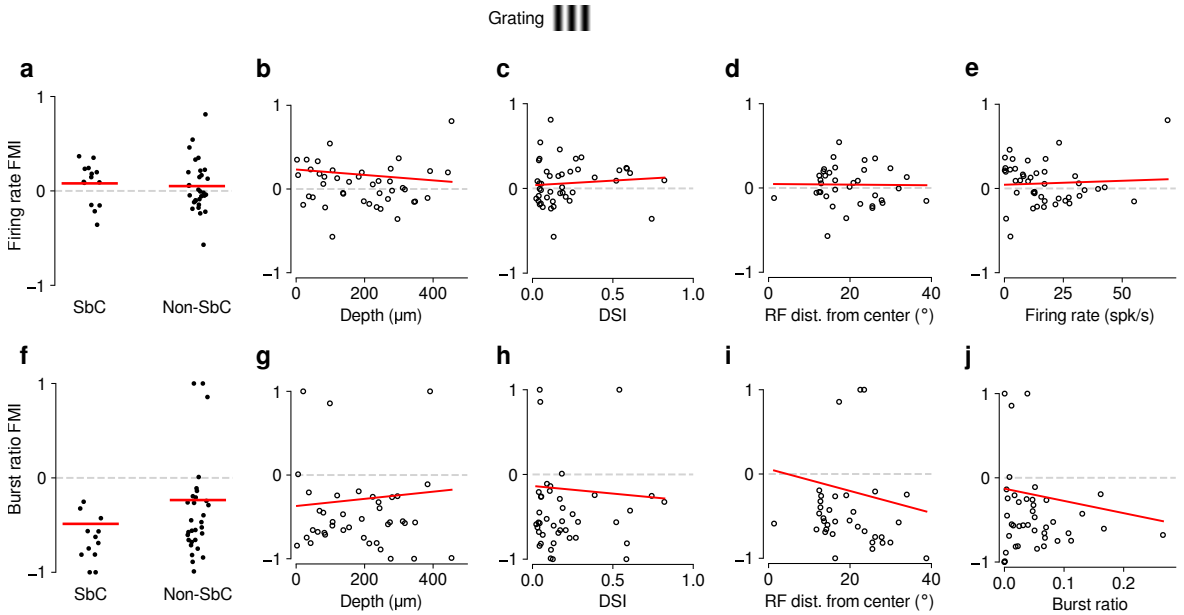

Figure 3-Supplement 1 As for movies (**Fig. 1-Supplement 3**), feedback effects during grating presentation are largely independent of functional cell type classification.
(**a–e**) Same as **Fig. 1-Supplement 3a–e** but for drifting gratings (0.08 (SbC) vs. 0.05 (non-SbC); LMM: $F_{1,42} = 0.12$, $p = 0.73$; depth: slope -0.00032 ± 0.0005; DSI: slope 0.11 ± 0.4; RF distance: slope -0.0004 ± 0.01; firing rate: slope 0.0009 ± 0.005). (**f–j**) Same as **Fig. 1-Supplement 3f–j** but for drifting gratings (-0.49 (SbC) vs. -0.24 (non-SbC); LMM: $F_{1,34.0} = 3.77$, $p = 0.061$; depth: slope 0.00043 ± 0.0012; DSI: slope -0.18 ± 0.6; RF distance: slope -0.013 ± 0.03; burst ratio: slope -1.5 ± 2.2).

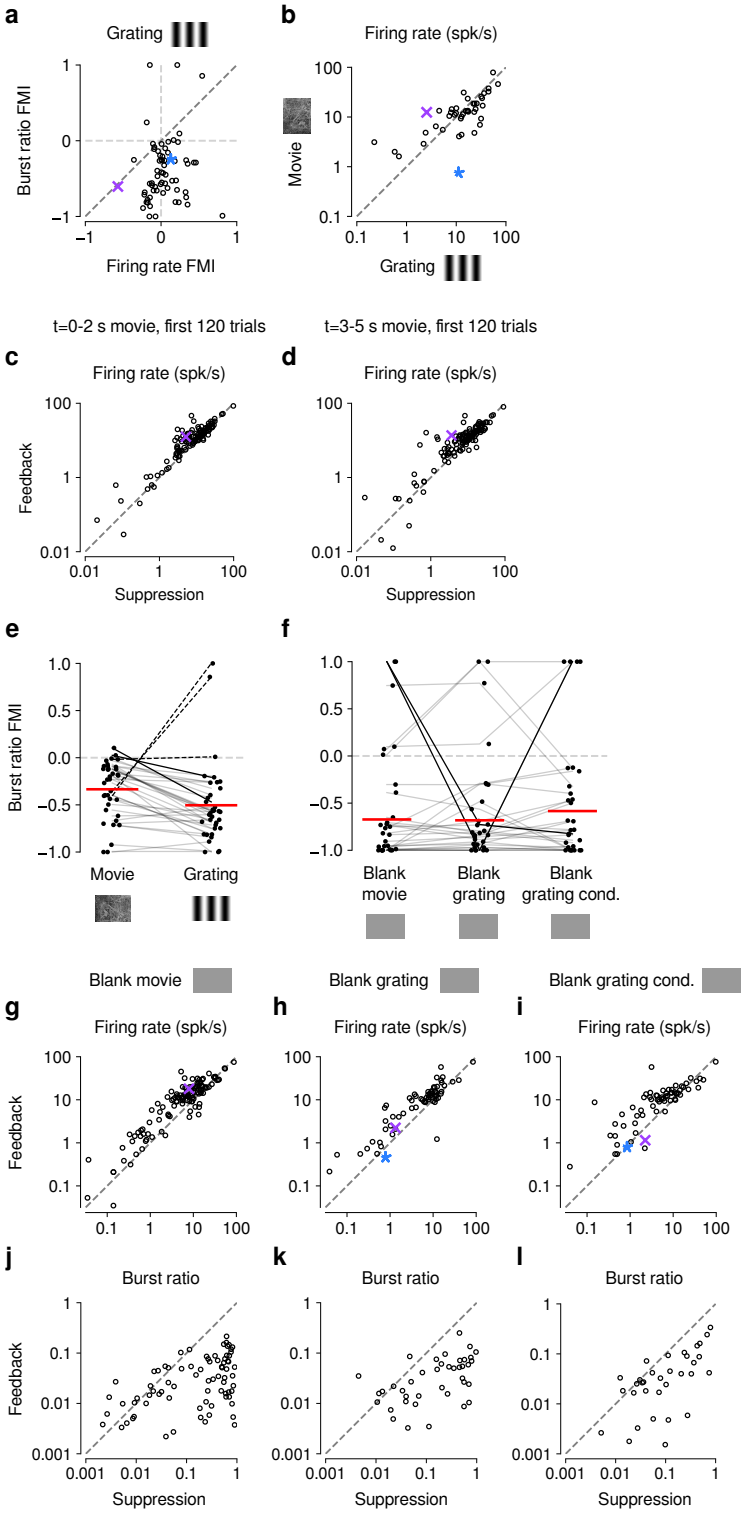
a
Grating
Burst ratio FMI
Firing rate FMI
b
Firing rate (spk/s)
Movie
Grating
t=0-2 s movie, first 120 trials
t=3-5 s movie, first 120 trials
c
Firing rate (spk/s)
Feedback
Suppression
d
Firing rate (spk/s)
Suppression
e
Burst ratio FMI
Movie
Grating
f
Blank movie
Blank grating
Blank grating cond.
Blank movie
Blank grating
Blank grating cond.
g
Firing rate (spk/s)
Feedback
h
Firing rate (spk/s)
i
Firing rate (spk/s)
j
Burst ratio
Feedback
Suppression
k
Burst ratio
Suppression
l
Burst ratio
Suppression

Figure 4-Supplement 1 (**Previous page**) Control analyses assessing the difference in CT feedback effects for gratings and movies.
(**a**) Similar to our results for movies (**Fig. 1-Supplement 2c**), CT feedback modulation of grating burst ratio was unrelated to CT feedback modulation of firing rate (LMM: slope of 0.029 ± 0.41). (**b**) With CT feedback intact, movies and gratings evoked firing rates of similar magnitude (13.3 spikes/s vs. 16.3 spikes/s, LMM: $F_{1,42} = 4.1$, $p = 0.05$). This rules out the possibility that larger CT feedback effects for movies are related to stronger firing rates already present in the baseline condition with CT feedback intact. (**c**) dLGN firing rates for movies were consistently higher during the CT feedback intact vs. V1 suppression condition, even when restricted to only the first 2 s and 120 trials of movie stimulation, for more direct comparison with grating stimulation (main effect of feedback, LMM: $F_{1,429.1} = 13.0$, $p = 0.0004$). (**d**) Same as (c), but for the last 2 s of movie stimulation. The effect of V1 suppression was indistinguishable during the first two and the last two seconds of the movie clips (interaction feedback $\times$ analysis window, LMM: $F_{1,429.1} = 0.54$, $p = 0.46$). Higher consistency of effects of V1 feedback suppression on firing rates for naturalistic movies thus cannot be explained by the longer duration or greater number of movie trials (5 s, 200 trials) than grating trials (2 s, 120 trials). (**e**) V1 suppression increases bursting more strongly during presentation of gratings than movies (burst ratio FMI of -0.34 (movies) vs. -0.5 (gratings); LMM: $F_{1,35} = 5.7$, $p = 0.023$). (**f**) V1 suppression increases bursting to a similar degree during short blank screen periods preceding movie and grating stimulus trials, and during blank grating conditions (burst ratio FMI of -0.67 (pre-movies) vs. -0.68 (pre-gratings) vs. -0.58 (blank grating condition); LMM: $F_{2,56} = 0.43$, $p = 0.65$). Burst ratio FMI depended only weakly on stimulus type (movie vs. grating, average of all blank conditions, LMM: $F_{2,126,2} = 2.8$, $p = 0.067$). (**g,h,i**) Comparison of firing rates during CT feedback vs. V1 suppression for short blank periods preceding movies and gratings, and during blank grating conditions. In all cases, CT feedback is associated with enhanced firing rates (blank pre-movies: firing rates 12.9 spikes/s (feedback) vs. 8.9 spikes/s (V1 suppression); LMM: $F_{1,178.7} = 24.2$, $p = 2.0 \times 10^{-6}$; blank pre-gratings: firing rates 11.5 spikes/s (feedback) vs. 7.9 spikes/s (V1 suppression); LMM: $F_{1,86.4} = 13.2$, $p = 0.0005$; blank grating condition: firing rates 11.4 spikes/s (feedback) vs. 8.5 spikes/s (V1 suppression); LMM: $F_{1,86.3} = 6.4$, $p = 0.01$). (**j,k,l**) Same as (g,h,i), but for burst ratio. In all cases, CT feedback is associated with less bursting (blank pre-movies: burst ratios 0.024 (feedback) vs. 0.22 (V1 suppression); LMM: $F_{1,185.7} = 96.5$, $p = 2.2 \times 10^{-16}$; blank pre-gratings: burst ratios 0.036 (feedback) vs. 0.22 (V1 suppression); LMM: $F_{1,93.0} = 38.1$, $p = 1.8 \times 10^{-8}$; blank grating condition: burst ratios 0.047 (feedback) vs. 0.14 (V1 suppression); LMM: $F_{1,83.0} = 24.4$, $p = 4.0 \times 10^{-6}$). (e,f) Red horizontal lines: means estimated by LMM.

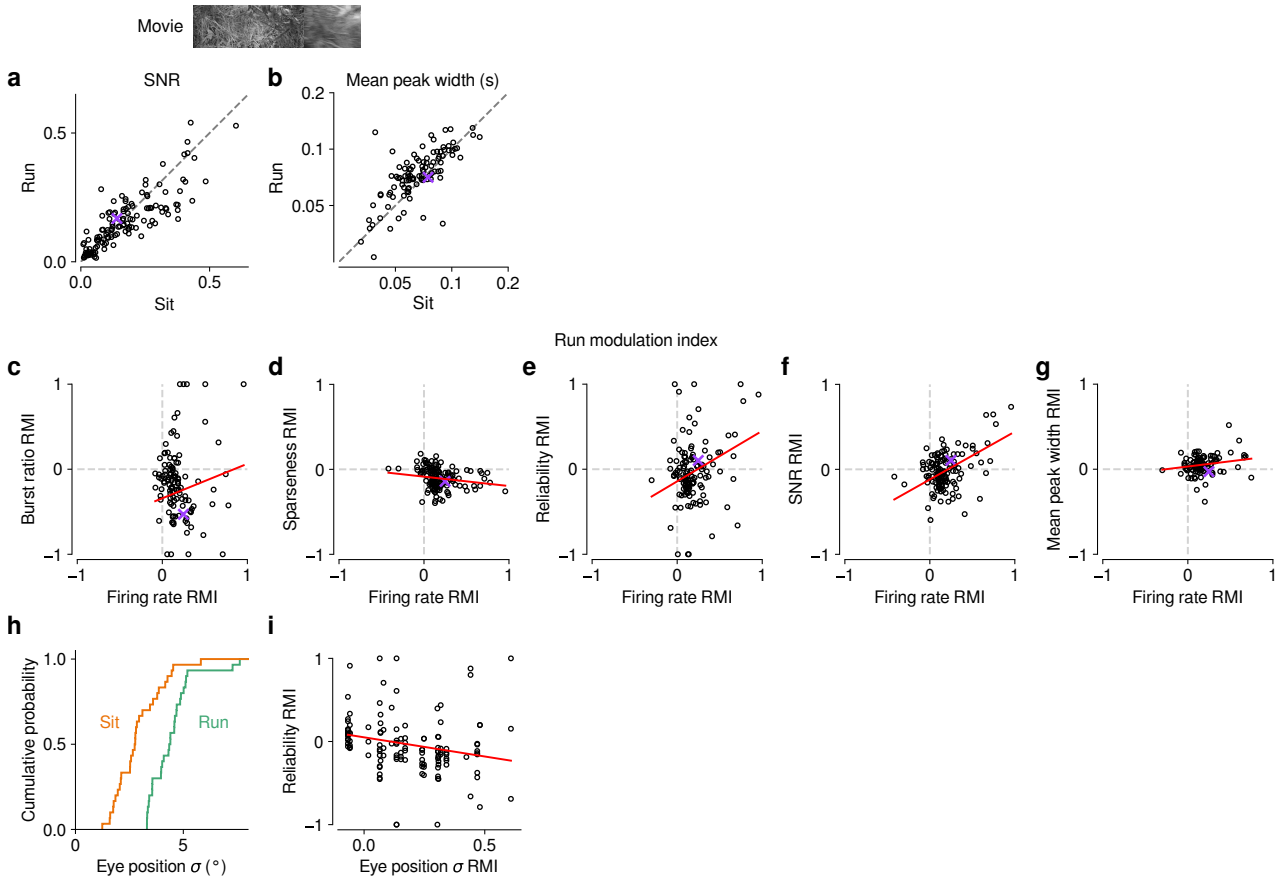

Figure 5-Supplement 1 Effects of locomotion on additional parameters of responses to naturalistic movie clips and relationship with firing rate.
(**a,b**) Comparison between trials with locomotion and stationary periods for (a) SNR [155] and (b) width of response peaks. During locomotion, SNR was lower (0.14 vs. 0.16, LMM: $F_{1,174.1} = 5.6$, $p = 0.019$) and mean peak width was broader (0.08 vs. 0.07, LMM: $F_{1,146.2} = 13.1$, $p = 0.0004$). (**c–g**) Relationship between locomotion effects (RMI) on firing rate of burst ratio (c), sparseness (d), reliability (e), SNR (f), and mean peak width (g). Locomotion-related changes in firing rate can to some degree account for the changes in reliability (LMM: slope of 0.59 ± 0.38) and SNR (LMM: slope of 0.56 ± 0.20). Slopes were non-significant for burst ratio (LMM: slope of 0.41 ± 0.43), sparseness (LMM: slope of -0.11 ± 0.11) and mean peak width (LMM: slope of 0.12 ± 0.14). (**h**) Cumulative distribution of trial-averaged eye-position standard deviation for stationary (*orange*) and locomotion (*green*) trials. Eye-position standard deviation was first calculated for each time point across trials, and then averaged across time points. In line with previous reports [80, 84], standard deviation of eye position was, on average, larger during locomotion than during stationary periods (4.4° vs. 2.9°, LMM: $F_{1,49} = 50.3$, $p = 4.8 \times 10^{-9}$, $N = 60$ experiments from 6 mice). (**i**) Locomotion-related trial-to-trial reliability co-varied with locomotion-related changes in eye position standard deviation (LMM: slope of -0.46 ± 0.38); however, the expected difference in reliability RMI corresponding to a 1 standard deviation difference in eye position σ RMI is -0.082, which is much smaller than the residual standard deviation of 0.28 unexplained by the regression. Therefore, changes in eye position during locomotion cannot account for most of the reduced reliability of responses during locomotion (**Fig. 5f**).